

Dust-driven Dynamos in Accretion Disks

P. M. Bellan

Applied Physics, Caltech, Pasadena CA 91125, USA

pbellan@caltech.edu

ABSTRACT

Magnetically driven astrophysical jets are related to accretion and involve toroidal magnetic field pressure inflating poloidal magnetic field flux surfaces. Examination of particle motion in combined gravitational and magnetic fields shows that these astrophysical jet toroidal and poloidal magnetic fields can be powered by the gravitational energy liberated by accreting dust grains that have become positively charged by emitting photo-electrons. Because a dust grain experiences magnetic forces after becoming charged, but not before, charging can cause irreversible trapping of the grain so dust accretion is a consequence of charging. Furthermore, charging causes canonical angular momentum to replace mechanical angular momentum as the relevant constant of the motion. The resulting effective potential has three distinct classes of accreting particles distinguished by canonical angular momentum, namely (i) “cyclotron-orbit”, (ii) “Speiser-orbit”, and (iii) “zero canonical angular momentum” particles. Electrons and ions are of class (i) but depending on mass and initial orbit inclination, dust grains can be of any class. Light-weight dust grains develop class (i) orbits such that the grains are confined to nested poloidal flux surfaces, whereas grains with a critical weight such that they experience comparable gravitational and magnetic forces can develop class (ii) or class (iii) orbits, respectively producing poloidal and toroidal field dynamos.

1. Introduction

Magnetohydrodynamically driven plasma jets having topology and dynamics analogous to astrophysical jets have been produced in laboratory experiments by Hsu & Bellan (2002); Bellan *et al.* (2005) and by Lebedev *et al.* (2005); see discussion by Blackman (2007). The feature of azimuthal symmetry, common to both the lab experiments and to real astrophysical jets, has important implications for the structure of the magnetic field. This is because an azimuthally symmetric magnetic field can be expressed using a cylindrical coordinate system $\{r, \phi, z\}$ as

$$\mathbf{B} = \frac{1}{2\pi} (\nabla\psi \times \nabla\phi + \mu_0 I \nabla\phi) \quad (1)$$

where the poloidal flux $\psi(r, z, t)$ is defined by

$$\psi(r, z, t) = \int_0^r 2\pi r' dr' B_z(r', z, t) \quad (2)$$

and the poloidal electric current $I(r, z)$ is defined by

$$I(r, z, t) = \int_0^r 2\pi r' dr' J_z(r', z, t). \quad (3)$$

The definition of $I(r, z)$ is consistent with Ampere's law for the toroidal field, since using $\nabla\phi = \hat{\phi}/r$ in Eq.1 gives the toroidal magnetic field to be

$$B_\phi = \frac{\mu_0 I}{2\pi r}. \quad (4)$$

Equations 1-3 describe the magnetic field and electric current distribution of *any* axisymmetric magnetic field. Because astrophysical jets are azimuthally symmetric, their magnetic field must be of the form prescribed by Eqs.1- 3 and, indeed, it is generally believed that astrophysical jets involve large-scale poloidal magnetic fields threading an accretion disk (e.g., see Livio (2002); Ferreira & Casse (2004)) and in addition, toroidal magnetic fields. Application of Ampere's law to Eq.1 shows that the poloidal and toroidal currents are respectively given by

$$\mathbf{J}_{pol} = \frac{1}{2\pi} \nabla I \times \nabla\phi \quad (5)$$

and

$$\mathbf{J}_{tor} = -\frac{r^2 \nabla \cdot (r^{-2} \nabla\psi)}{2\pi\mu_0} \nabla\phi \quad (6)$$

showing that poloidal magnetic fields are produced by a toroidal electric current and toroidal magnetic fields are produced by a poloidal current; toroidal vectors are those vectors in the ϕ direction and poloidal vectors are those in any combination of the r and z directions.

Knowledge of the two stream-function quantities $I(r, z, t)$ and $\psi(r, z, t)$ is thus necessary and sufficient to determine the complete vector magnetic field and the complete vector current density.

The term ‘magnetic axis’ has traditionally been assigned different meanings in the respective contexts of astrophysics and laboratory toroidal magnetic confinement devices (e.g., tokamaks, reversed field pinches, or spheromaks). Specifically, a local maximum in r - z space of $\psi(r, z)$ is called a magnetic axis in the context of toroidal confinement devices whereas the z symmetry axis of the magnetic field is called the magnetic axis in the context of astrophysics. To avoid confusion, we will call the location of a maximum of $\psi(r, z)$ the poloidal flux magnetic axis. Poloidal magnetic field lines follow level contours of ψ and so one can envision the projection of the magnetic field in the r - z plane as being like a set of roads, each at a different altitude, encircling a mountain peak at a specific r - z location which is the poloidal flux magnetic axis (also called an O-point). Since a toroidal current at infinity is not physical, and since the net magnetic flux enclosed by a circle with infinite radius must vanish as field lines cannot go to infinity, ψ must vanish at infinity. Furthermore, mathematical regularity of physical quantities requires ψ to vanish on the z axis (Lewis & Bellan 1990). Thus, a non-trivial ψ can only be finite in the region $0 < r < \infty$, $-\infty < z < \infty$. The simplest situation of physical interest is therefore where ψ has a single maximum in the r - z plane. We will consider this situation, namely a single poloidal field magnetic axis with $\psi(r, z)$ symmetric with respect to z . This situation has been previously considered by Lovelace *et al.* (2002) and implies via Eq.6 that a toroidal current circulates in an accretion disk to produce the poloidal magnetic field

$$\mathbf{B}_{pol} = \frac{1}{2\pi} \nabla \psi \times \nabla \phi. \quad (7)$$

An inescapable feature of this topology is that because $\nabla \psi = 0$ at the maximum of ψ , i.e., at the poloidal field magnetic axis, the poloidal magnetic field has a null on the poloidal field magnetic axis. In the $z = 0$ plane, the poloidal flux ψ thus starts from zero at $r = 0$, increases to a maximum at the poloidal field magnetic axis, and then decays to zero as $r \rightarrow \infty$.

We define a to be the radius of the poloidal field magnetic axis. In addition, we define $\langle B_z \rangle$ to be the *spatially-averaged* axial magnetic field linked by the poloidal field magnetic axis and ψ_0 to be the value of the poloidal magnetic flux at the poloidal field magnetic axis, so

$$\langle B_z \rangle = \frac{\int_0^a dr 2\pi r B_z(r, 0)}{\int_0^a dr 2\pi r} = \frac{\psi_0}{\pi a^2}. \quad (8)$$

The axial field $B_z = (2\pi r)^{-1} \partial \psi / \partial r$ reverses sign at $r = a$ and the radial field $B_r = -(2\pi r)^{-1} \partial \psi / \partial z$ reverses sign at $z = 0$. An analytic representation for a physically realizable

generic flux function satisfying all these properties is derived in Appendix A. This generic flux function is

$$\psi(r, z) = \frac{27 (r/a)^2 \psi_0}{8 \left(\left(\frac{r}{a} + \frac{1}{2} \right)^2 + \left(\frac{z}{a} \right)^2 \right)^{3/2}} \quad (9)$$

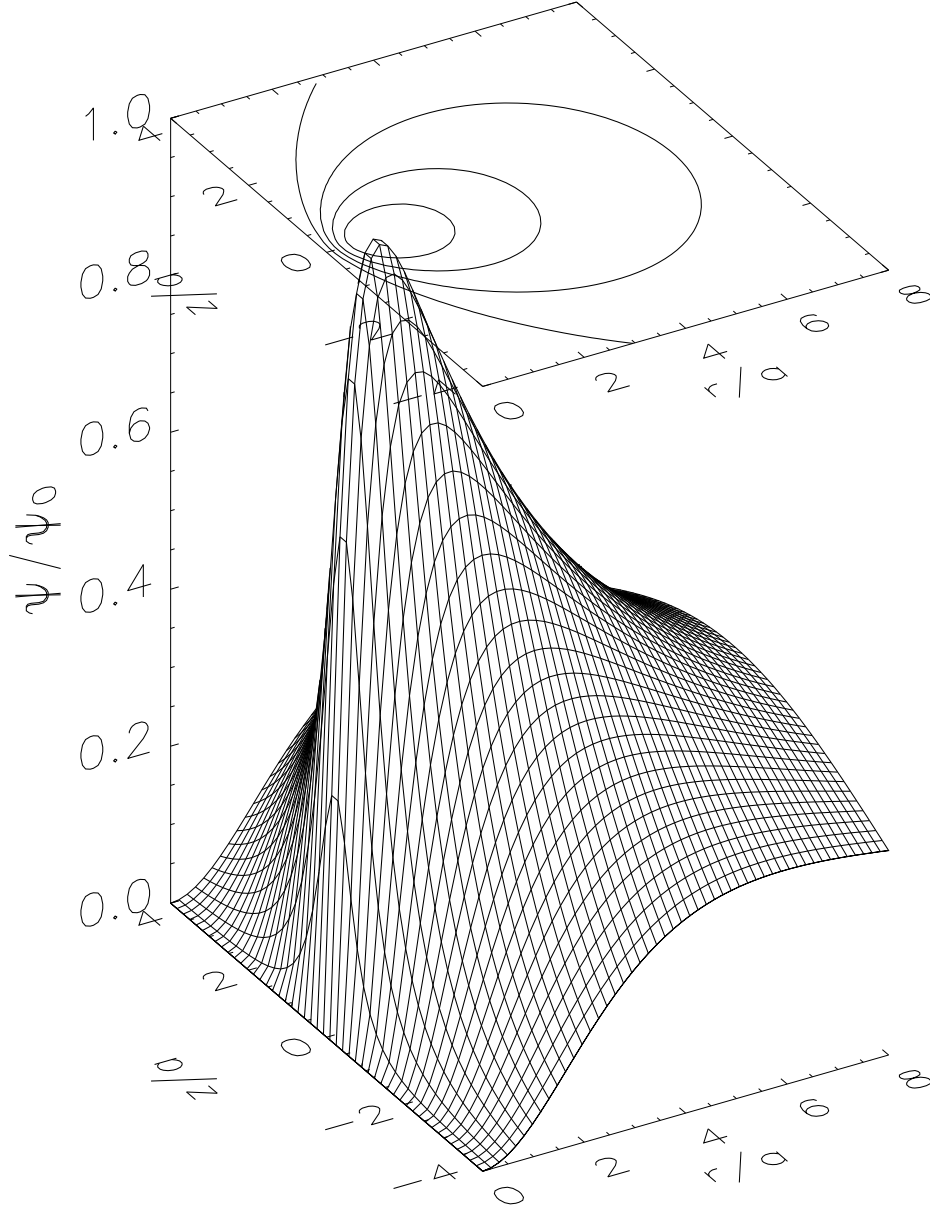
and has the properties that (i) $\psi(r, z)$ has a maximum value of ψ_0 at $r = a, z = 0$, (ii) $\psi \sim r^2$ for $r \ll a$ and $z = 0$, (iii) $\psi \sim r^{-1}$ for $r \gg a, z$ and (iv) for $r \ll a/2$ or $r \gg a$ and for $z \gg a$ the contours of ψ are identical to the contours of the poloidal flux produced by a current loop located at $r = a/2, z = 0$. This flux function thus encompasses simpler models which assume a uniform axial magnetic field B_z ; these simpler models would correspond to the $r, z \ll a$ region here since in this region $\psi \sim r^2$ which corresponds to having a uniform axial magnetic field B_z . This flux function could also be used to describe the far-field of a dipole by assuming that $r, z \gg a$. Since any real axial magnetic field must always be generated by a toroidal current located at some finite radius, any real situation will have a poloidal flux function qualitatively similar to Eq.9. The flux function prescribed in Eq.9 is similar in essence to the flux function used in Fig.1 of Lovelace *et al.* (2002).

Figure 1 plots $\psi(r, z)$ as prescribed by Eq.9 and shows that $\psi(r, z)$ has its maximum at the poloidal field magnetic axis $r = a, z = 0$. This flux function corresponds to a smoothly varying toroidal current density prescribed by Eq.6 concentrated in the vicinity of $r = a, z = 0$. Since for $z = 0$ and small r , this function has the asymptotic dependence $\psi \simeq 27\psi_0 (r/a)^2$, it corresponds to an approximately uniform axial magnetic field $B_z \simeq 27\psi_0/\pi a^2$ for $r, z \ll a$. The $r \ll a$ inner-region B_z is thus 27 times stronger than the average B_z field between 0 and a . The total toroidal current \mathcal{I}_ϕ associated with the generic flux function given by Eq.9 is calculated in Appendix B using the integral form of Ampere's law and found to be

$$\mathcal{I}_\phi = \frac{27\psi_0}{\pi a \mu_0} . \quad (10)$$

The laboratory jets involve the mutual interaction between poloidal and toroidal magnetic fields powered by laboratory capacitor banks. The jet acceleration mechanism results from the pressure of the toroidal magnetic field inflating flux surfaces associated with the poloidal magnetic field. The question arises as to what powers the toroidal and poloidal magnetic fields in an actual astrophysical situation. Existing models of astrophysical jets are based on the magnetohydrodynamic (MHD) approximation of plasma behavior and typically assume (i) the poloidal field is pre-existing and (ii) the toroidal field results from a rotating accretion disk twisting up this assumed primordial poloidal field. The purpose of this paper is to present an alternate model wherein it is postulated that the toroidal and poloidal field result instead from a non-MHD dusty plasma dynamo mechanism that converts the gravitational energy of infalling dust grains into an electrical power source that drives

Fig. 1.— Plot of the normalized generic flux function $\psi(r, z)/\psi_0$ in coordinates normalized to the radius of the poloidal field magnetic axis, that is to the radial position of the maximum of $\psi(r, z)$. Contours of iso-surfaces shown on top; these correspond to projection of poloidal magnetic field onto r - z plane.



poloidal and toroidal electric currents creating the respective toroidal and poloidal fields. A brief outline of how infalling charged dust can drive poloidal currents has been presented in Bellan (2007).

This model obviously requires existence of sufficient infalling dust to provide the jet power. Since the dust-to-gas mass ratio in the Interstellar Medium (ISM) is 1%, one might be tempted to argue that any jet driven by the proposed dust infall mechanism would be limited to having less than 1% of the power available from infalling gas, a constraint that would contradict observations. However, in Bellan (2008) (to be referred to as Paper I), we showed that the dust-to-gas mass ratio in a molecular cloud can be substantially enriched compared to the ISM value (e.g., the dust to gas mass ratio in a molecular cloud could be enriched 20-fold compared to the 1% ISM value). This enrichment occurs because accreting dust slows down much more in proportion to its initial velocity than does accreting gas so that the density amplification resulting from dust slowing down is much greater than the corresponding density amplification of gas.

The condition for the toroidal magnetic field to inflate the poloidal magnetic field and create a jet can be expressed as

$$\frac{\mu_0 I}{\psi} > \lambda \quad (11)$$

where λ is a parameter of the order of the inverse characteristic linear dimension in the radial direction. The ratio I/ψ can be thought of as the ratio of the electric current flowing along a flux tube to the magnetic flux content of the flux tube and is proportional to the twist of the magnetic field. Equation 11, well-established in spheromak formation physics (Barnes *et al.* 1990; Jarboe 1994; Geddes *et al.* 1998; Bellan 2000; Hsu & Bellan 2005), is essentially a statement that jet expansion (i.e., poloidal field inflation) occurs when the toroidal magnetic field pressure force $\sim B_\phi^2 A_1$ acting on area A_1 exceeds the restraining force $B_z^2 A_2$ of the poloidal magnetic field ‘tension’ acting on area A_2 . Here A_1 and A_2 are not exactly the same because the toroidal and poloidal fields do not act over the same areas. The equivalence between Eq. 11 and the condition $B_\phi^2 > B_z^2 A_2/A_1$ is seen by substituting $\mu_0 I = 2\pi a B_\phi$ from Ampere’s law and $\psi \sim B_z \pi a^2$ in Eq.11.

Paper I divided the regions of interest into successively smaller concentric regions and considered dust and gas behavior in the outermost regions. Simultaneous gas and dust accretion were considered and it was shown that the dust could be considered as a perturbation on the gas, so that the gas accretion problem could be solved first without considering dust and then the solution of this gas accretion problem could be used as an input for the dust accretion problem. Below is a listing showing which regions were considered in Paper I, which are considered in this paper, and which will be considered in a future paper; the nominal radii scales and star mass are from Table 3 in Paper I:

ISM scale (considered in Paper I): The outermost scale is that of the Interstellar Medium (ISM). The ISM has a gas density $\sim 10^7 \text{ m}^{-3}$, a dust-to-gas mass ratio of 1 percent, a gas temperature $T_g^{ISM} \sim 100 \text{ K}$, and is optically thin. The ISM is assumed to be spatially uniform and to bound a molecular cloud having radius $r_{edge} \sim 10^5 \text{ a.u.}$

Molecular cloud scale (considered in Paper I): The molecular cloud scale has much higher density than the ISM and is characterized by force balance between gas self-gravity and gas pressure. The molecular cloud scale is sub-divided into a large, radially non-uniform low-density outer region and a small, approximately uniform, high-density inner core region. Clouds have a characteristic scale given by the Jeans length $r_J \sim 1.4 \times 10^4 \text{ a.u.}$ The radial dependence of gas density is provided by the Bonnor-Ebert sphere solution which acts as the outer boundary of the Bondi accretion scale.

Bondi accretion scale (considered in Paper I): The Bondi accretion scale is $\sim r_B \sim 4.3 \times 10^3 \text{ a.u.}$ which is sufficiently small that gas self-gravity no longer matters so equilibrium is instead obtained by force balance between gas pressure and the gravity of a central object assumed to be a star having mass $M \sim 0.4 M_\odot$. The Bondi scale is sub-divided into three concentric radial regions: an outermost region where the gas flow is subsonic, a critical transition radius at exactly r_B where the flow is sonic, and an innermost region where the gas flow is free-falling and supersonic.

Collisionless dusty plasma scale (considered in this paper): Free-falling dust grains collide with each other in one of the above scales and coagulate to form large-radius grains which are collisionless and optically thin. The optically thin dust absorbs UV photons from the star, photo-emits electrons and becomes electrically charged. The charged dust grains are subject to electromagnetic forces in addition to gravity. Motions of charged dust grains relative to electrons result in electric currents with associated poloidal and toroidal magnetic fields [see preliminary discussion in Bellan (2007)]. This region is assumed to have a scale of $10 - 10^3 \text{ a.u.}$ and corresponds to the scale of a , the radius of the poloidal magnetic field axis. It is assumed that a distributed toroidal current peaked at a nominal radius a is responsible for producing a poloidal field having the generic profile given in Fig.1.

Jet scale (to be considered in a future publication): The electric currents interact with the magnetic fields to produce magnetohydrodynamic forces that drive astrophysical jets in a manner consistent with Eq.11 and analogous to that reported in Hsu & Bellan (2002, 2005) and Bellan *et al.* (2005). This region is assumed to have a scale $\ll 10^3 \text{ a.u.}$, possibly as small as a few a.u. and will involve a deformation of the generic poloidal field profile given in Fig.1 because of the pressure of toroidal magnetic field inflating the poloidal flux surfaces.

2. Outline of model

We will show how infalling collisionless dust grains can develop special three dimensional orbits suitable for sustaining both toroidal and poloidal dynamos. This result is obtained by considering Hamiltonian particle dynamics in the combination of the gravitational field of a star with mass M and a three-dimensional axisymmetric magnetic field topology consistent with previous models of magnetically driven astrophysical jets [e.g., Lovelace (1976), Li *et al.* (2001), Lovelace *et al.* (2002), and Lynden-Bell (2003)]. The reason why dust grains develop these special orbits will be shown to be due to charging of dust grains via photo-emission of electrons. The analysis involves using Hamiltonian mechanics to generalize the centrifugal potential so as to include magnetic force, i.e., the Störmer effective potential is used. Störmer potentials have been previously used for investigating auroral particles (Störmer 1955), electron and ion motion in the magnetosphere (Shebalin 2004; Lemaire 2003) and most recently, charged dust grain motion in the magneto-gravitational fields of Saturn and Jupiter (Dullin *et al.* 2002; Mitchell *et al.* 2003). Störmer potentials are also commonly used to characterize particle orbits in tokamaks (Rome & Peng 1979) and Störmer potentials were found to be important in the MHD-driven jet experiment reported by Tripathi *et al.* (2007). We will restrict the analysis to showing how toroidal and poloidal field dynamos can be sustained in steady state by these special Hamiltonian particle orbits; the much more complicated problem of how a dynamo grows from a seed magnetic field will not be addressed here. These special orbits are quite different from conventional cyclotron orbits. As reviewed in Appendix C a dynamo cannot be sustained by particles executing cyclotron orbits because cyclotron orbits and associated drifts are diamagnetic, i.e., create magnetic fields that oppose the field in which the particle is orbiting.

The importance of a Hamiltonian analysis can be appreciated by considering the gedanken experiment where the charge to mass ratio of a particle in a combined gravitational-magnetic field is assumed to be increased from zero (neutral particle) to that of an electron or ion. The particle will thus make a transition from Kepler to cyclotron orbital motion. The details of how this transition occurs have been examined by Bellan (2007) in the context of uniform-magnetic-field orbits restricted to a plane. The present paper will address this issue in the more general context of three dimensional particle orbits in a spatially non-uniform three dimensional magnetic field having dipole-like topology appropriate for an accretion disk; similar dipole topology has been previously invoked for accretion disks by Lovelace *et al.* (2002). Our analysis identifies five distinct classes of orbits and shows that the class to which a given charged particle belongs depends both on its charge to mass ratio and on the circumstances under which the charged particle was created from an initially neutral particle. The interaction between the distinct symmetries of the magnetic and gravitational fields removes the isotropy of the incident neutral particles existent prior to charging so

that the newly formed charged particles separate into groups having qualitatively different types of orbits. Some orbits correspond to a simple accretion, some involve accretion and production of a dynamo driving toroidal current, and some involve accretion and a dynamo driving poloidal current. The type of orbit a charged particle develops depends on both the angular momentum and the angle of incidence of the parent neutral particle.

The paper is organized with the goal of being concise while also realizing that some readers may not be familiar with the concepts of adiabatic versus non-adiabatic orbits, Speiser orbits, Störmer effective potentials, and how conservation of canonical angular momentum results in confinement of an adiabatic particle to the vicinity of a poloidal flux surface. Rather than reviewing these concepts in an introductory section, they are instead discussed in appendices.

3. Reduction of collisionality due to dust agglomeration

Paper I showed that dust grains are collisionally decoupled from gas in the ISM and then become collisionally coupled to gas in the Bonner-Ebert and Bondi regions of a molecular cloud. Because of the spherical focusing of the dust and gas inflows, the dust density increases to a level such that dust-dust collisions become important. When dust grains collide with each other they may agglomerate to form larger dust grains. Przygodda *et al.* (2003) and van Boekel *et al.* (2003) have reported direct observational evidence of grain growth in circumstellar disks while, in addition, Jura (1980), Miyake & Nakagawa (1993), Pollack *et al.* (1994), D’Alessio *et al.* (2001), and Dullemond & Dominik (2005) provided detailed calculations showing a strong tendency for dust grain growth when dust grains collide with each other. This agglomeration will increase the dust grain radius r_d while keeping the dust mass density ρ_d constant. We will consider first how this agglomeration affects dust-gas collisions and then how it affects dust-dust collisions.

Since the mean free path is much larger than the grain radius, the drag force on a dust grain due to collisions with gas molecules is of the Epstein-type and given by (Lamers & Cassinelli 1999)

$$F_{drag} = -(u_d - u_g)\rho_g\sigma_d\sqrt{c_g^2 + (u_d - u_g)^2} \quad (12)$$

where c_g is the gas thermal velocity, u_d is the dust grain velocity, σ_d is the dust grain cross-sectional area, and u_g is the mean velocity of the gas (i.e., the fluid velocity). In the innermost Bondi region where flow is supersonic, we may approximate $c_g \simeq 0$ and work in a frame moving with u_g by defining $\Delta u_d = u_d - u_g$. The dust equation of motion in this frame is thus

$$m_d \frac{d\Delta u_d}{dt} = - (\Delta u_d)^2 \rho_g \sigma_d. \quad (13)$$

Defining ξ to be distance in the direction of dust motion so $\Delta u_d = d\xi/dt$, Eq.13 can be recast as

$$\frac{d\Delta u_d}{d\xi} \Delta u_d = - (\Delta u_d)^2 \sigma_d \frac{\rho_g}{m_d}. \quad (14)$$

Integration gives

$$\Delta u_d(\xi) = \Delta u_d(0) \exp(-\xi/l_{dg}) \quad (15)$$

where the dust-gas collision mean free path is

$$l_{dg} = \frac{m_d}{\rho_g \sigma_d}. \quad (16)$$

Since the dust cross-section and mass are given respectively by

$$\sigma_d = \pi r_d^2 \quad (17)$$

and

$$m_d = \frac{4\pi r_d^3 \rho_d^{int}}{3} \quad (18)$$

where ρ_d^{int} is the intrinsic density of a dust grain, the dust-gas collision mean free path can be expressed as

$$l_{dg} = \frac{4\rho_d^{int}}{3\rho_g} r_d \quad (19)$$

which shows that dust agglomeration increases the dust-gas mean free path and so will tend to make dust collisionless with respect to gas.

Let us now consider how agglomeration affects dust-dust collisions. We first note that the condition for dust-dust collisions to be significant is closely related to the condition for the dust to be optically thick: if l is the characteristic length of a configuration, the condition for collisions to be significant is $\rho_d \sigma_d l / m_d > 1$ whereas the condition for the dust to be optically thick is $Q_{eff} \rho_d \sigma_d l / m_d > 1$ where Q_{eff} is an extinction efficiency parameter that depends on the ratio of the dust radius to the light wavelength. The dust-dust collision mean free path is thus

$$l_{dd} = \frac{m_d}{\rho_d \sigma_d} = \frac{4\rho_d^{int}}{3\rho_d} r_d \quad (20)$$

so if, as argued in Paper I, the dust mass density ρ_d has been enriched to be a significant fraction of the gas mass density ρ_g , the dust-dust collision mean free path l_{dd} will be the same order of magnitude as the dust-gas mean free path l_{dg} . Agglomeration will thus tend

to increase both the dust-dust and dust-gas collision mean free paths, and furthermore will cause the dust to become optically thin. We will assume that dust grains agglomerate when the dust number density $n_d = \rho_d/m_d$ becomes sufficiently large for dust-dust collisions to occur and that this agglomeration results in an increase in r_d until the dust grains become collisionless and optically thin again. We will not attempt to follow the dynamics of the agglomeration process, relying instead on the analysis in the papers cited above. Our starting point then will be assuming the existence of collisionless dust grains exposed to star light, having radius r_d larger than in the ISM, and as discussed in Paper I, having a dust to gas mass density ratio substantially enriched compared to the 1% value in the ISM.

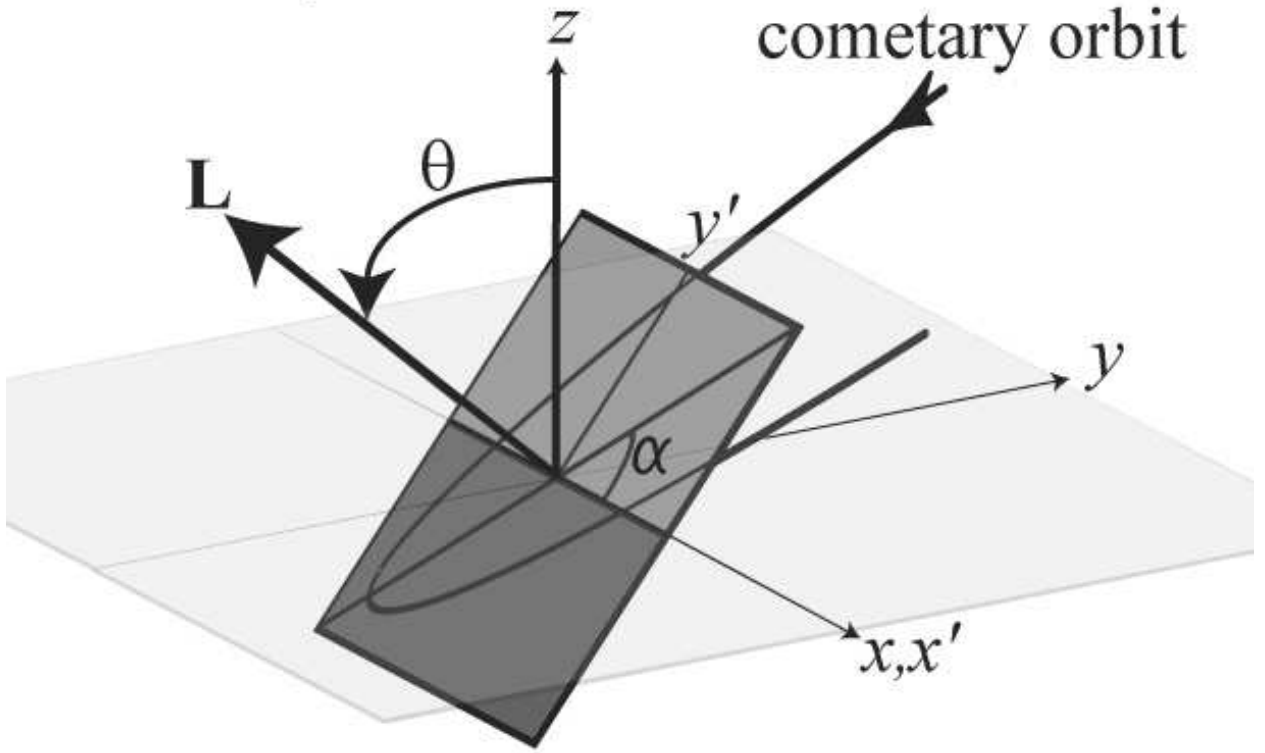
4. Review: Neutral particle motion in a gravitational field

For reference and in order to define terms to be used later in a more complex context, we first review the elementary problem of the motion of a neutral particle of mass m in the gravitational field of a star of mass M . The particle we have in mind could be a dust grain with radius r_d sufficiently large to be collisionless over the distance from its starting point to the star.

The equations governing the motion of this neutral particle are spherically symmetric whereas the motions of a charged particle in an azimuthally symmetric electromagnetic field are cylindrically symmetric. An axisymmetric magnetic field is assumed to exist in the lab frame and the z axis is defined by the direction of this magnetic field at the origin. Although the neutral particle trajectory is unaffected by this magnetic field, we nevertheless use the magnetic field coordinate system to define the lab frame. Depending on what is being emphasized, the lab frame will be characterized by either a cylindrical coordinate system $\{r, \phi, z\}$ or by a Cartesian coordinate system $\{x, y, z\}$ so that $x = r \cos \phi$, and $y = r \sin \phi$. Because the force is central, the neutral particle angular momentum vector $\mathbf{L} = m\mathbf{r} \times \dot{\mathbf{r}}$ is invariant and so the neutral particle moves in an orbital plane normal to \mathbf{L} . The lab and orbital planes are sketched in Fig.2. The x axis of the lab frame is defined to be in the direction of the unit vector $\hat{x} = \hat{z} \times \mathbf{L}/L$ and the y axis of the lab frame is defined to be in the direction of the unit vector $\hat{y} = \hat{z} \times (\hat{z} \times \mathbf{L}/L)$. The orbital plane is tilted with respect to the lab frame by an angle θ about the x axis. The x' axis of the orbital frame is defined to be coincident with the x axis of the lab frame and the y' axis of the orbital plane is an uptilted version of the y axis of the lab frame.

$\theta = 0$ corresponds to prograde motion in the lab frame (i.e., the neutral particle moves in the same sense as the toroidal current that produces the magnetic field B_z on the z axis), $\theta = \pi$ corresponds to retrograde motion in the lab frame, and $\theta = \pi/2$ corresponds to a polar

Fig. 2.— Lab frame has Cartesian coordinates x, y, z and the magnetic field is axisymmetric with respect to the lab frame z axis. The orbital plane of a neutral particle is normal to the neutral particle angular momentum vector \mathbf{L} which is tilted by an angle θ with respect to the z axis. The orbital plane Cartesian coordinates are x', y' where the x' axis is coincident with the x axis. The neutral particle makes a circular Kepler, elliptical Kepler, or cometary orbit in its orbital plane (cometary orbit shown).



orbit. For purposes of following the trajectory in the orbital plane it is convenient to use cylindrical coordinates ρ, η defined in the orbital plane such that $x' = \rho \cos \eta$ and $y' = \rho \sin \eta$. The Hamiltonian for a neutral particle moving in its orbital plane can then be written as

$$H = \frac{1}{2}mv_\rho^2 + \frac{L^2}{2m\rho^2} - \frac{mMG}{\rho} \quad (21)$$

where

$$L = m\rho v_\eta, \quad (22)$$

the magnitude of the mechanical angular momentum vector, is an invariant positive scalar. The Kepler angular frequency at a reference radius a is defined as

$$\Omega_0 = \sqrt{MG/a^3}. \quad (23)$$

The value of a is chosen to be the radius of the poloidal magnetic field axis. Normalized quantities are defined as

$$\begin{aligned} \bar{\rho} &= \rho/a, \tau = \Omega_0 t, \bar{v}_\rho = \frac{v_\rho}{\Omega_0 a} \\ \bar{L} &= \frac{L}{m\Omega_0 a^2}, \quad \bar{H} = \frac{H}{m\Omega_0^2 a^2}. \end{aligned} \quad (24)$$

Equation 21 can then be expressed in dimensionless form as

$$\bar{H} = \frac{\bar{v}_\rho^2}{2} + \frac{\bar{L}^2}{2\bar{\rho}^2} - \frac{1}{\bar{\rho}}. \quad (25)$$

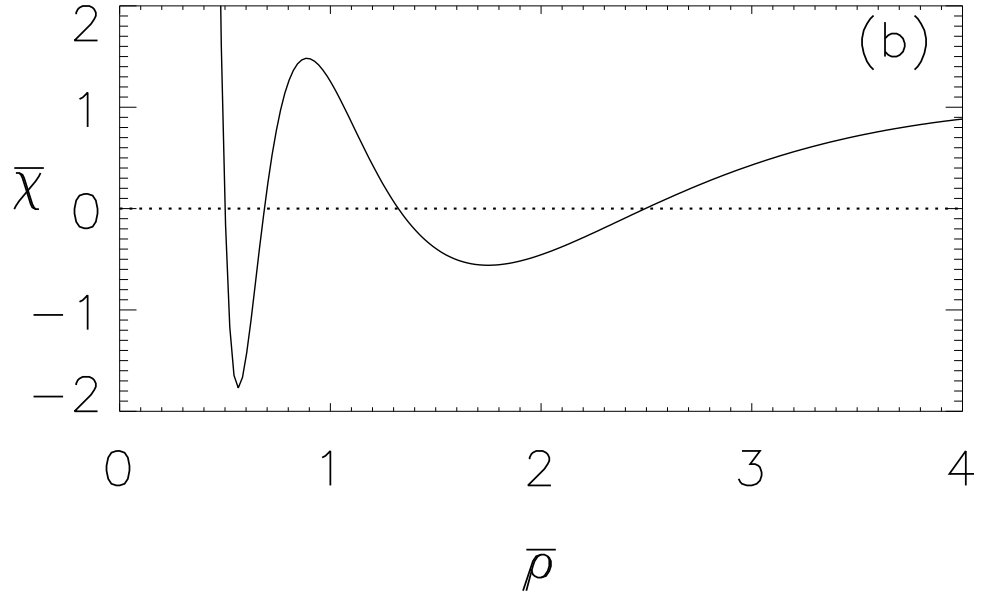
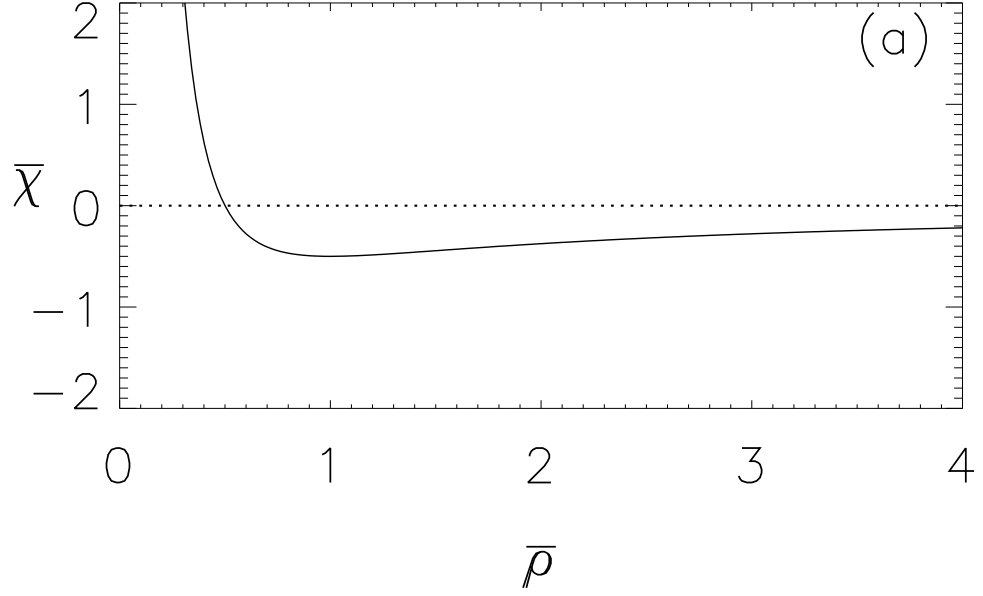
The last two terms depend on $\bar{\rho}$ and so constitute an effective potential

$$\bar{\chi}(\bar{\rho}) = \frac{\bar{L}^2}{2\bar{\rho}^2} - \frac{1}{\bar{\rho}}. \quad (26)$$

This effective potential depends parametrically on \bar{L} which is a property of the particle and not the environment. Two different particles at the same position but having different values of \bar{L} will have different effective potentials and so march to a “different drummer”. This “different drummer” concept will re-appear later in a more elaborate fashion when the motion of charged particles is considered.

$\bar{\chi}(\bar{\rho})$ attains its minimum value $\chi_{\min} = -1/2\bar{L}^2$ at the normalized radius $\bar{\rho} = \bar{L}^2$. A particle with energy equal to this minimum has $\bar{v}_\rho = 0$ and therefore has a circular orbit with angular frequency $d\eta/d\tau = L/\Omega_0 m a^2 = \bar{L}/\bar{\rho}^2$. Hence, if $\bar{L} = 1$ the minimum-energy particle traces out a circular Kepler orbit with $d\eta/d\tau = 1$ and has an energy $\bar{H} = -1/2$. A particle with energy $-1/2 < \bar{H} < 0$ cannot escape to infinity and so has a bounded elliptical Kepler orbit. The effective potential prescribed by Eq.26 for a particle with $\bar{L} = 1$ is shown in Fig.3(a).

Fig. 3.— (a) Effective potential for a neutral particle having $\bar{L} = 1$; (b) effective potential for a charged particle with appropriate values of canonical angular momentum and poloidal flux function.



Reflection (pericenter) of a particle occurs when $\bar{v}_\rho = 0$ in which case Eq.25 gives

$$\bar{\rho}_{pericenter} = \frac{\bar{L}^2}{1 + \sqrt{1 + 2\bar{L}^2\bar{H}}}. \quad (27)$$

Reflection at the pericenter can be considered to be the consequence of a potential barrier preventing the particle from accessing the region $\bar{\rho} < \bar{\rho}_{pericenter}$; the effective potential in the inaccessible region exceeds the total available energy. Thus an unbounded particle with $\bar{L} = 1$ also has the effective potential shown Fig. 3(a), but unlike the bounded $\bar{H} = -1/2$ Kepler particle, the unbounded particle reflects from the pericenter potential barrier and so has a cometary orbit.

In order for an incoming unbound particle to access a given $\bar{\rho}$ without being reflected at some larger radius, the condition that \bar{v}_ρ^2 cannot be negative gives the constraint on angular momentum that

$$\bar{L}^2 < 2\bar{\rho}^2\bar{H} + 2\bar{\rho}. \quad (28)$$

Since a particle with zero angular momentum will simply fall into the central object, in order for a particle to be both unbounded and able to access the radius $\bar{\rho}$ its angular momentum is constrained to lie in the range

$$0 < \bar{L}^2 < 2\bar{\rho}^2\bar{H} + 2\bar{\rho}. \quad (29)$$

Solution of the equation of motion (Goldstein 1950) shows that the orbit can be expressed as

$$\frac{1}{\bar{\rho}} = \frac{1 - \sqrt{1 + 2\bar{L}^2\bar{H}} \cos(\eta - \alpha)}{\bar{L}^2} \quad (30)$$

where α , which we call the clock angle in the orbital plane, is the angle between the symmetry line of the orbit (the line passing through the central object and the pericenter position) and the lab frame x axis (which is also the x' axis of the orbital plane).

The Cartesian orbit coordinates $\bar{x}' = \bar{\rho} \cos \eta$ and $\bar{y}' = \bar{\rho} \sin \eta$ in the orbital plane (denoted by a prime to distinguish this plane from the lab frame) are

$$\begin{aligned} \bar{x}' &= \frac{\bar{L}^2 \cos \eta}{1 - \sqrt{1 + 2\bar{L}^2\bar{H}} \cos(\eta - \alpha)} \\ \bar{y}' &= \frac{\bar{L}^2 \sin \eta}{1 - \sqrt{1 + 2\bar{L}^2\bar{H}} \cos(\eta - \alpha)} \end{aligned} \quad (31)$$

If the effective potential had a different shape, say the shape shown in Fig.3(b) with $\bar{\chi} \rightarrow 0$ at large $\bar{\rho}$, then a particle with $\bar{H} \geq 0$ could be trapped in one of the two minima of this effective potential. However, a particle coming from infinity would still be unbounded and would just reflect from some potential barrier. The inability of a static Hamiltonian system to trap a particle coming from infinity is independent of the shape of the Hamiltonian and results from the intrinsic time reversibility of Hamiltonian dynamics.

5. Comparison of gravitational/magnetic forces to Poynting-Robertson force and to radiation pressure

The analysis in this paper is based on the assumption that the trajectory of charged dust grains results primarily from a competition between gravitational and magnetic forces with the possibility that in certain situations electrostatic forces and collisional drag can also be important. Two other types of forces, namely those due to the Poynting-Robertson effect and due to radiation pressure, also exist and so it is important to check to see if these additional forces need to be taken into account. This will be done by making a comparison with the nominal magnetic force on a charged dust grain. The magnetic force depends on the strength of the magnetic field, a quantity which has been estimated in self-consistent fashion in Paper III to be in the range 10^{-8} to 10^{-6} T (i.e., 0.1 to 10 mG) for a nominal YSO jet-disk system where the dust grains have coagulated to a nominal radius $r_d = 3 \mu\text{m}$. This estimate of the magnetic field is in rough order of magnitude agreement with measurements reported by Chrysostomou *et al.* (1994), by Roberts *et al.* (1997) and by Itoh *et al.* (1999), and also is in agreement with the expectation that the magnetic fields in a disk jet system should be much stronger than the nominal 10^{-10} T (i.e., 1 μG) magnetic fields of the ISM.

The radiation pressure acting on a dust grain at a distance r from a star with luminosity L is

$$P_{rad} = \frac{L}{4\pi r^2 c} Q_{rad}(r_d) \quad (32)$$

where $Q_{rad}(r_d)$ is the efficiency with which the photons are absorbed/reflected by the dust grain. This pressure results in a radial outwards force $F_{rad} = P_{rad}\sigma_d$. If the dust grain radius is much larger than λ_{rad} the wavelength of the radiation, then $Q_{rad} \simeq 1$ whereas if the dust grain radius is much smaller than the wavelength of the radiation then $Q_{rad} \sim (\lambda_{rad}/r_d)^4 \ll 1$. The nominal $r_d \sim 3 \mu\text{m}$ dust grains assumed here are much larger than the nominal light wavelength and so $Q_{rad} \sim 1$.

Since the gravitational force $F_g = mMG/r^2$ is also in the radial direction, the force due to radiation pressure and gravity compete; the ratio of radiation pressure force to gravitational force on a dust grain is

$$\alpha = \frac{LQ_{rad}\sigma_d}{4\pi c m_d M G} = \frac{3}{16\pi} \frac{L}{M G \rho^{int} c} \frac{Q_{rad}(r_d)}{r_d} \quad (33)$$

where Eqs.17 and 18 have been used. Assuming $r_d = 3 \mu\text{m}$, nominal luminosity $L = L_\odot = 4 \times 10^{26}$ watts, $M = M_\odot$, intrinsic dust density $\rho^{int} = 2 \times 10^3 \text{ kg m}^{-3}$, and $Q_{rad}(r_d) = 1$ gives $\alpha = 10^{-1}$ so radiation pressure can be ignored compared to gravitational force.

The force on a dust grain due to the Poynting-Robertson effect is smaller by a factor v/c compared to the radiation pressure force, is in the toroidal direction, opposes the Keplerian

orbital motion $v_K = \sqrt{MG/r}$, and so constitutes a drag force

$$F_{PR} = F_G \alpha \frac{v_K}{c} = \frac{Q_{rad} r_d^2}{4c^2} \sqrt{\frac{MGL^2}{r^5}}. \quad (34)$$

The toroidal component of the magnetic force acting on a charged particle has magnitude

$$F_{mag} = Ze v_r B \quad (35)$$

where Z is the charge. The grains typically have non-circular trajectories with v_r being of the order of the Kepler velocity v_K so $F_{mag} \sim Ze v_K B$. The ratio of Poynting-Robertson force to magnetic force is thus

$$\frac{F_{PR}}{F_{mag}} = \frac{F_G}{F_{mag}} \alpha \frac{v_K}{c}. \quad (36)$$

Since the dust grains are assumed to be in a regime where they are acted on by magnetic forces which are at least comparable to gravitational forces, i.e., $F_{mag} \gtrsim F_G$ and since $\alpha \ll 1$ and $v_K/c \ll 1$ it is seen that the force due to Poynting-Robertson effect is negligible compared to magnetic forces and so the Poynting-Robertson effect, like radiation pressure, may be neglected.

6. Electromagnetic particle Hamiltonian with gravity

Hamilton-Lagrange methods are mathematically equivalent to the particle equation of motion and so describe all physically allowed orbits (e.g., cyclotron, drift, Speiser, etc.). Furthermore, because the Hamilton-Lagrange approach clarifies effects of spatial symmetries, deeper insight into orbital dynamics is obtained than provided by direct integration of the equation of motion. Direct integration nevertheless provides insight as well by providing an independent verification of the predictions of Hamilton-Lagrange methods. This two-pronged approach (Hamilton-Lagrange and direct orbit integration) provides a powerful method for examining particle motion in non-adiabatic situations.

The Lagrangian of a particle with mass m_σ and charge q_σ in the combination of an axisymmetric electromagnetic field and the spherically symmetric gravitational potential of a mass M central object is

$$\begin{aligned} \mathcal{L} = & \frac{m_\sigma}{2} \left(v_r^2 + r^2 \dot{\phi}^2 + v_z^2 \right) \\ & + q_\sigma \left(r \dot{\phi} A_\phi(r, z, t) + v_z A_z(r, z, t) \right) \\ & - q_\sigma V(r, z, t) + \frac{m_\sigma M G}{(r^2 + z^2)^{1/2}} \end{aligned} \quad (37)$$

where $V(r, z, t)$ is the electrostatic potential and a gauge with $A_r = 0$ is assumed. The canonical angular momentum is

$$P_\phi \equiv \frac{\partial \mathcal{L}}{\partial \dot{\phi}} = m_\sigma r^2 \dot{\phi} + q_\sigma r A_\phi \quad (38)$$

and, since $\mathbf{B}_{pol} = \nabla \times [(2\pi r)^{-1} \psi \hat{\phi}] = \nabla \times (A_\phi \hat{\phi})$ implies $\psi = 2\pi r A_\phi$, the canonical angular momentum can be expressed in terms of the poloidal magnetic flux as

$$P_\phi = m_\sigma r^2 \dot{\phi} + \frac{q_\sigma}{2\pi} \psi(r, z, t). \quad (39)$$

Lagrange's equation $\dot{P}_\phi = \partial \mathcal{L} / \partial \phi$ provides the important result that

$$P_\phi = \text{const.}, \quad (40)$$

i.e., P_ϕ is a constant of the motion because the system is axisymmetric. In the limit of a strong magnetic field, the second term in Eq.39 dominates the first and leads to the constraint that a particle orbit must stay very nearly on a surface of constant ψ ; this is the basis for particle confinement in axisymmetric toroidal fusion devices (tokamaks, reversed field pinches, and spheromaks). Any deviation of a particle from a constant ψ surface is a consequence of finite m_σ . When finite m_σ is taken into account, it is seen that the particle must stay within a poloidal Larmor radius of a constant ψ surface, where poloidal Larmor radius means the cyclotron radius evaluated using the local poloidal field magnitude. Equation 39 may be solved for $\dot{\phi}$ to give

$$\dot{\phi} = \frac{P_\phi - \frac{q_\sigma}{2\pi} \psi(r, z, t)}{m_\sigma r^2}. \quad (41)$$

The corresponding Hamiltonian is

$$H = \frac{m_\sigma}{2} (v_r^2 + r^2 \dot{\phi}^2 + v_z^2) + q_\sigma V(r, z, t) - \frac{m_\sigma M G}{(r^2 + z^2)^{1/2}}. \quad (42)$$

By using Eq.41 to substitute for $\dot{\phi}$ in Eq.42, the Hamiltonian can be expressed as

$$\begin{aligned} H = & \frac{m_\sigma}{2} (v_r^2 + v_z^2) \\ & + \frac{(P_\phi - \frac{q_\sigma}{2\pi} \psi(r, z, t))^2}{2m_\sigma r^2} \\ & + q_\sigma V(r, z, t) - \frac{m_\sigma M G}{(r^2 + z^2)^{1/2}}. \end{aligned} \quad (43)$$

We now consider situations where ψ is time-independent and $V = 0$ so the Hamiltonian reduces to

$$H = \frac{m_\sigma}{2} (v_r^2 + v_z^2) + \frac{(P_\phi - \frac{q_\sigma}{2\pi} \psi(r, z))^2}{2m_\sigma r^2} - \frac{m_\sigma M G}{\sqrt{r^2 + z^2}}. \quad (44)$$

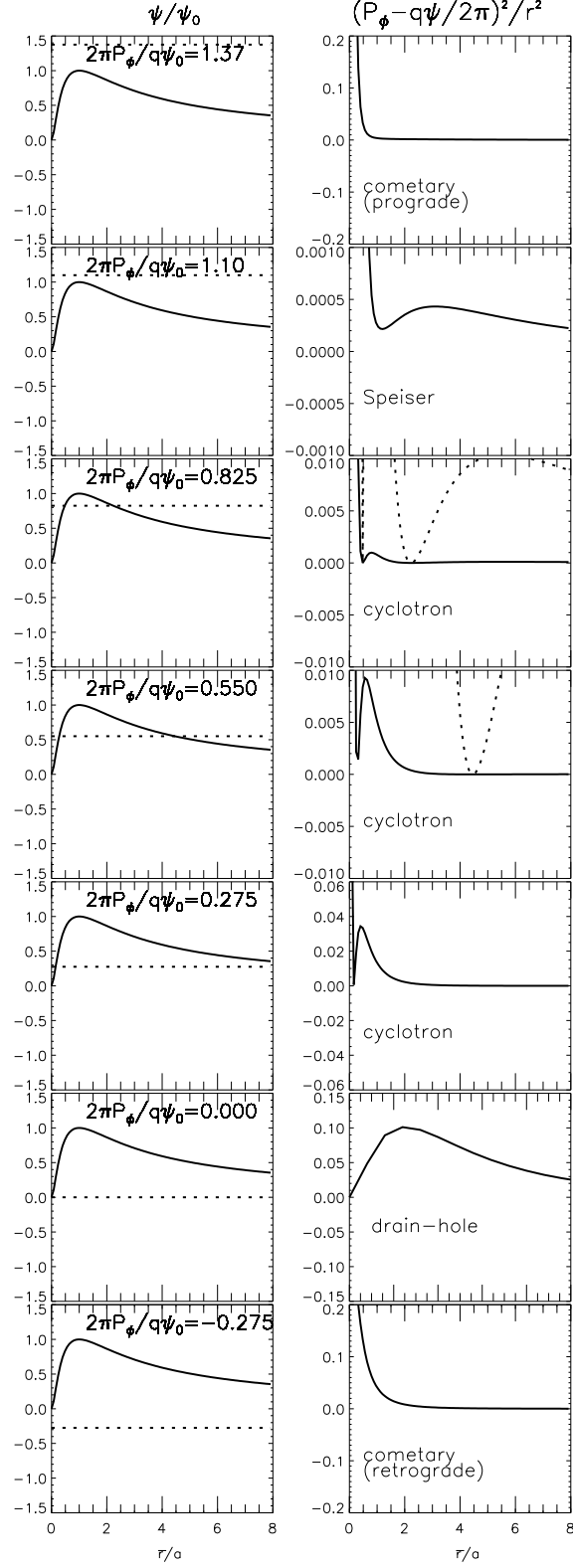
Since the Lagrangian does not explicitly depend on time, $H = \text{const.}$ and the particle energy is conserved. In the $q_\sigma\psi = 0$ limit, P_ϕ reduces to the mechanical angular momentum $p_\phi = mr^2\dot{\phi} = m\mathbf{r} \times \dot{\mathbf{r}} \cdot \hat{\mathbf{z}} = L \cos \theta$ in which case the dynamics reduces to the neutral particle orbital mechanics reviewed in Sec.4. Thus, if $q_\sigma\psi = 0$ bounded orbits correspond to $H < 0$ and circular Kepler orbits correspond to H having the minimum value of the effective potential well. Unbounded $q_\sigma\psi = 0$ orbits correspond to $H \geq 0$. Note that $p_\phi = L \cos \theta$ is a signed quantity, unlike L .

If $q_\sigma\psi$ is finite then $(P_\phi - q_\sigma\psi(r, z)/2\pi)^2/2m_\sigma r^2$ is the appropriate term which contributes to the effective potential. This term, called the Störmer potential, manifests a variety of qualitatively different spatial profiles depending on the relationship between P_ϕ and $q_\sigma\psi(r, z)/2\pi$. These profiles are shown in Fig.4 for a sequence of decreasing values of P_ϕ . Very large positive P_ϕ gives prograde orbits similar to unmagnetized prograde cometary orbits and very large negative P_ϕ gives retrograde orbits similar to unmagnetized retrograde cometary orbits; in both these cases the strong centrifugal repulsion at small r causes the particle to have an unbounded cometary orbit.

Caption for Fig. 4

Left: Plot of $\psi(r, z)/\psi_0$ v. r/a for $z = 0$ with sequence of values of $2\pi P_\phi/q\psi_0$ shown as dotted line. Right: Corresponding dependence of effective potential term $(P_\phi - q\psi(r, z)/2\pi)^2/r^2$ showing that potential wells develop at locations where $2\pi P_\phi/q\psi_0$ intersects $\psi(r, z)/\psi_0$. These wells correspond to cyclotron motion if the intersection is away from the maximum of ψ and to Speiser orbits if the intersection is at or near the maximum of ψ . A potential well at $r = 0$ develops if $P_\phi = 0$ as seen in the sixth set of plots from top; this results in drain-hole orbits. Dotted line in right-hand second plot from top has the vertical scale multiplied by 100 to enable visualization of the outer minimum and the dotted line on the third plot from the top has the vertical scale multiplied by 2000 times. Note changes of scale in right-hand plots.

Fig. 4.— caption on previous page



On the other hand, if P_ϕ and $q_\sigma\psi(r, z)/2\pi$ have comparable magnitude, complex effective potential structures can result. For example if at some location P_ϕ equals $q_\sigma\psi(r, z)/2\pi$ then $(P_\phi - q_\sigma\psi(r, z)/2\pi)^2/2m_\sigma r^2$ vanishes at this location, giving a *localized minimum* in the overall effective potential.

If two separated positions exist where P_ϕ equals $q_\sigma\psi(r, 0)/2\pi$ then two distinct minima exist, but if only one position exists where P_ϕ equals $q_\sigma\psi(r, 0)/2\pi$ then only one minimum exists. The former situation occurs when P_ϕ lies somewhere between 0 and the maximum of ψ and leads to cyclotron orbits with associated grad- B and curvature drifts; in this case Eq.41 shows that the sign of $\dot{\phi}$ oscillates as the particle oscillates back and forth across the minimum of the effective potential, and the orbit is a cyclotron orbit. The situation of only one minimum occurs when the value of P_ϕ is approximately the maximum of $q_\sigma\psi/2\pi$ and gives Speiser orbits ($\dot{\phi}$ has fixed sign and the orbit is paramagnetic). For a review of the distinction between the diamagnetism of cyclotron orbits (and associated grad- B and curvature drifts) and the paramagnetism of Speiser orbits see Appendix C.

Yet another situation is where $P_\phi = 0$. Because $\psi \sim r^2$ at small r , this special case removes the singularity of $(P_\phi - q_\sigma\psi(r, 0)/2\pi)^2/2m_\sigma r^2$ at $r = 0$ and so eliminates centrifugal force repulsion altogether. The $P_\phi = 0$ case gives trajectories which spiral down towards the central object while crossing magnetic field lines; part of the magnetic force cancels the centrifugal force so all that is left is gravity and a residual inward magnetic force. This situation is completely different from either cyclotron orbits or Speiser orbits and has only been previously discussed in the more limited context of two dimensional situations (Bellan 2007). Finally, there is also the special situation discussed by Schmidt (1979) where $P_\phi = -r^2 q_\sigma (2\pi)^{-1} \partial(\psi/r)/\partial r$ in which case the charged particle executes an axis-encircling cyclotron orbit. While possible in principle, axis-encircling cyclotron orbits will be not be considered here because they would correspond to particles having extreme energies (e.g., a cyclotron radius of many a.u.).

Thus, there are five qualitatively distinct types of feasible trajectories depending on the relationship between P_ϕ and $q_\sigma\psi/2\pi$. As labeled in Fig.4 and in order of descending signed value of the invariant P_ϕ as shown by dashed horizontal line in left column of this figure, these are:

1. prograde centrifugally dominated orbits [P_ϕ much larger than the peak of $q_\sigma\psi(r, z)/2\pi$]
2. Speiser orbits [P_ϕ just grazes the peak of $q_\sigma\psi(r, z)/2\pi$]
3. cyclotron orbits [P_ϕ well below the peak of $q_\sigma\psi(r, z)/2\pi$ but much greater than zero]

4. $P_\phi = 0$ orbits [which we will call “drain-hole” orbits for reasons to be discussed later], and
5. retrograde centrifugally dominated orbits [P_ϕ negative and much less than zero)].

In the above list, we have removed the constraint that $z = 0$ so, for example, in case #3 (cyclotron orbits), the locations in the r - z plane where P_ϕ and $q_\sigma\psi(r, z)/2\pi$ are equal corresponds to a specific closed curve in the r - z plane; i.e., a specific ψ iso-surface as shown in the projection of $\psi(r, z)$ at the top of Fig. 1.

The various possible values of P_ϕ can be considered as the different “drummers” that dictate the effective potentials governing the motion of different particles located at the same position. A related example of this different “drummers” situation has been reported by Tripathi *et al.* (2007) and involves two particles at the same location having velocities with equal magnitudes but opposite directions; the two particles have such extremely different effective potentials that one particle is expelled from a magnetic flux tube (hill-shaped effective potential) whereas the other remains in the flux tube (valley-shaped effective potential).

6.1. Mechanism for accretion of collisionless particles

Accretion is the process of converting unbounded orbits (i.e., cometary orbits) into bounded orbits. Accretion of a collisionless neutral particle is clearly impossible if such a particle is governed by dynamics of a time-independent Lagrangian because converting an unbounded orbit into a bounded orbit would require changing the particle energy H and such a change is forbidden for a particle having a Lagrangian that does not explicitly depend on time.

We now postulate an accretion mechanism as follows: *photo-emission acts as an effective switch which alters the form of the Hamiltonian equation governing particle dynamics.* The particle energy H and mechanical angular momentum $mr^2\dot{\phi}$ do not change during the switching, but after photo-emission has occurred, H and $mr^2\dot{\phi}$ become parameters in a *different Hamiltonian system* which has a different topography of potential barriers. For example, photo-emission can transform the neutral particle effective potential shown in Fig.3(a) into the charged particle effective potential shown in Fig.3(b).

The switching is postulated to occur when an incident neutral dust grain absorbs sufficient energetic photons from the star. The photon absorption causes the dust grain to photo-emit electrons and therefore become positively charged (Lee 1996; Sickafoose *et al.* 2000). The photo-emitted electrons become free electrons equal in number to the dust grain

charge Z . The photo-emission process has effectively caused the initial neutral dust grain to disintegrate into a single heavy positively charged fragment (the charged dust grain) and Z light negatively charged fragments (the photoelectrons). The motion of each fragment is governed by the Hamiltonian for a charged particle and this Hamiltonian is considerably different in form from the Hamiltonian that governed the neutral particle motion.

The charge q_d of a dust grain charged by photo-emission is given by

$$\frac{q_d}{4\pi\epsilon_0 r_d} \approx W_{photon} - W_{wf} \quad (45)$$

where W_{photon} is the energy in eV of an incident photon that causes photo-emission of a primary photo-electron and W_{wf} is the work-function in eV of the material (Shukla & Mamun 2002). Lee (1996) has shown that the effective photon energy is $W_{photon} \simeq 8$ eV for nominal solar parameters and the effective work function of typical dust is $W_{wf} \simeq 6$ eV so that the energy of emitted photo-electrons is ~ 2 eV.

Combination of Eqs. 18 and 45 show that the dust charge to mass ratio will be

$$\frac{q_d}{m_d} = \frac{3\epsilon_0 (W_{photon} - W_{wf})}{\rho_d^{int} r_d^2} \quad (46)$$

which will be many of orders of magnitude smaller than the charge to mass ratios of electrons or ions. The number Z of charges on a dust grain will be

$$Z = \frac{4\pi\epsilon_0 r_d (W_{photon} - W_{wf})}{e}. \quad (47)$$

Charging a dust grain to q_d takes a finite time interval, but for simplicity we will assume that this charging occurs at a single time defined as $t = 0$. Charging will not change either the instantaneous position or velocity of a particle.

Photo-emission at $t = 0$ therefore decomposes an incident neutral dust grain into positive and negative product particles each inheriting the same position and velocity at $t = 0_+$ that the neutral dust grain had at $t = 0_-$. Position and velocity can consequently be considered to be continuous functions at $t = 0$ so the canonical angular momentum with which a newly formed charged particle is endowed is

$$\begin{aligned} P_\phi &= m_\sigma r_*^2 \dot{\phi}_* + q_\sigma \psi(r_*, z_*)/2\pi \\ &= L_\sigma \cos \theta + q_\sigma \psi(r_*, z_*)/2\pi \end{aligned} \quad (48)$$

where the subscript $*$ denotes the value of a coordinate at the instant of charging, i.e., at $t = 0$. For simplicity we assume that photo-emission occurs when the distance between the incident neutral and the central object is at some critical spherical radius R_* so that

charging and the setting of $t = 0$ occurs when the particle crosses the surface of the fictitious R_* sphere, i.e., when $r = r_*$ and $z = z_*$ are such that

$$r_*^2 + z_*^2 = R_*^2. \quad (49)$$

Depending on the value of L_σ , the angle of inclination θ , the magnitude of q_σ , and the value of $\psi(r_*, z_*)$, all possible finite values of P_ϕ can occur, including positive, negative, and zero. The r - z plane topography of the effective potential can change completely from what it was at $t = 0_-$ because the centrifugal force potential $p_\phi^2/2mr^2$ responsible for the neutral particle potential barrier at small r is replaced by the Störmer term $(P_\phi - q_\sigma\psi(r, z))^2/2\pi mr^2$. Figure 4 demonstrates that variation of particle mass and variation of the incoming orbit plane inclination angle θ results in a range of p_ϕ , q_d values and hence a range of P_ϕ values corresponding to cyclotron, “drain-hole”, Speiser, or cometary orbits. If the new orbit is cyclotron, drain-hole, or Speiser, then photo-emission has prevented the particle from returning to infinity, i.e., the particle has accreted. Photo-emission changes the “rules of the game” by effectively erecting a new potential barrier which traps a previously unbound particle. The “old game” (i.e., neutral particle Keplerian motion as reviewed in Sec.4) did not depend on particle mass or θ , but the “new game” does and leads to a mass- and θ -dependent sorting of incoming charged grains and their associated photo-emitted electrons into qualitatively different classes of orbits.

This process whereby neutral particles enter a magnetic field from outside, become charged, and then become subject to magnetic forces is called ‘neutral beam injection’ in the context of tokamak physics and ‘pickup’ in the context of solar physics. Neutral beam injection is used routinely for tokamak heating and current drive (Simonen *et al.* 1988; Akers *et al.* 2002). Pickup is important in the solar wind (Gloeckler & Geiss 2001), in planetary atmospheres (Hartle & Killen 2006), and in producing source particles for cometary rays (Ellison *et al.* 1998). However, to the best of the author’s knowledge, charging of incoming neutral particles has not been previously proposed as a means for accreting matter around a star and instead accretion of matter around a star has always been argued to be the result of the viscosity of neutral particles, i.e., collisions of neutral particles with each other, as discussed for example in Lynden-Bell & Pringle (1974), Shakura & Sunyaev (1976), and Pringle (1981). The viscosity-based neutral particle accretion models suffer from not knowing what to do with the angular momentum of incident particles; this issue has motivated substantial work on developing the rather complicated non-linear turbulence-based magneto-rotational instability model as a means for transporting excess angular momentum outwards. In contrast, the model proposed here inherently accounts for angular momentum and so does not need any “add-on turbulence” to transport angular momentum outwards.

Trapping via photo-emission has the remarkable feature that the special class of charged

particles created with zero canonical angular momentum will spiral all the way down to the central object. These $P_\phi = 0$ (drain-hole) particles falling towards $r = 0$ are in what is effectively a loss cone in canonical angular momentum space. The drain-hole particle motion constitutes a gravity-driven dynamo (Bellan 2007) because the accumulation of these particles near $r = 0$ produces a radially outward electric field while their flow produces a radially inward electric current (a dynamo is characterized by having opposed internal electric field and electric current). Since $J_r = -(2\pi r)^{-1} \partial I / \partial z$ (see Eq.5), creation of this radially inward current which is symmetric with respect to z implies creation of an anti-symmetric function $I(r, z)$ which in turn implies creation of an anti-symmetric toroidal field B_ϕ (see Eq.4). Equally remarkable, particles for which P_ϕ is near the maximum of $q_\sigma \psi / 2\pi$ develop Speiser-type *paramagnetic* orbits in the vicinity of $r = a$, $z = 0$ and so can constitute the toroidal current that produces the poloidal flux (see discussion of Speiser orbit paramagnetism in Appendix C). The creation of Speiser-orbit particles is conceptually similar to toroidal current drive in a tokamak via tangential neutral beam injection (Simonen *et al.* 1988). Because the drain-hole and Speiser dynamos are both axisymmetric, both violate the essential claim of Cowling’s anti-dynamo theorem (Cowling 1934) that axisymmetric dynamos cannot exist. This violation is not a problem because Cowling’s theorem is based on MHD and so does not take into account drain-hole or Speiser orbits.

The Hamiltonian for an incoming neutral dust grain of mass m_n can be written as

$$H = \frac{m_n v_r^2}{2} + \frac{m_n v_\phi^2}{2} + \frac{m_n v_z^2}{2} - \frac{m_n M G}{\sqrt{r^2 + z^2}}. \quad (50)$$

This neutral dust grain absorbs energetic photons at $t = 0$, photo-emits Z free electrons, and consequently becomes positively charged with a charge of Z . The mass of the neutral is related to the mass m_+ of the positively charged dust grain by $m_n = m_+ + Z m_e$ where m_e is the electron mass. Prior to this charging process, Eq.50 can be written as

$$H = \frac{(m_+ + Z m_e) v_r^2}{2} + \frac{(m_+ + Z m_e) v_\phi^2}{2} + \frac{(m_+ + Z m_e) v_z^2}{2} - \frac{(m_+ + Z m_e) M G}{\sqrt{r^2 + z^2}} \quad (51)$$

so the positively charged dust grain with mass m_+ and the Z electrons can each be thought of as executing identical neutral-type orbits before photo-emission occurs.

At the instant before charging, the neutral particle mechanical angular momentum is

$$p_\phi = m_n r_*^2 \dot{\phi}_*. \quad (52)$$

At the instant after charging the newly created positively charged dust grain and its associated photo-emitted electrons all have the same values of r_* and $\dot{\phi}_*$. The canonical angular

momentum of the positively charged dust grain will therefore be

$$P_\phi^+ = m_+ r_*^2 \dot{\phi}_* + Ze\psi(r_*, z_*)/2\pi \quad (53)$$

and the canonical momentum of each associated electron will be

$$P_\phi^e = m_e r_*^2 \dot{\phi}_* - e\psi(r_*, z_*)/2\pi. \quad (54)$$

The initial neutral dust grain will be called the “parent” particle while the positively charged dust grain resulting from photo-emission and its associated Z photo-emitted electrons will be called “child particles” that are “siblings” of each other. The set of child particles resulting from the charging of a specific neutral dust grain will be called a “family”. The canonical momenta P_ϕ^+ and P_ϕ^e are now the appropriate orbit invariants for $t > 0$ whereas the mechanical angular momenta $m_\sigma r^2 \dot{\phi}$ of the individual siblings will *not* be invariant for $t > 0$. Although the mechanical angular momentum of an individual sibling is not conserved, the total mechanical angular momentum of the family is conserved since summing Eq.53 and Z times Eq.54 gives $[p_\phi]_{family} = P_\phi^+ + ZP_\phi^e$ where $[p_\phi]_{family} = m_n r_*^2 \dot{\phi}$ is the sum of the mechanical angular momentum of the charged dust grain and all its sibling electrons. Because the siblings can physically separate from each other, the mechanical angular momentum $[p_\phi]_{family}$ is not a locally defined quantity and so is not a constant of the motion of either a single particle or, as in ideal hydrodynamics, of a fluid element. However, *the mechanical angular momentum of the entire system is conserved* because the angular momentum of each family is globally conserved.

The kinetic energy of each sibling at the instant before photo-emission is the same as the value at the instant after photo-emission. If H is decomposed into the contributions from the various siblings, it is seen that each sibling’s H_σ is the same before and after photo-emission. Assuming zero electrostatic potential for now, but allowing the child particle to be at arbitrary z , the Hamiltonian of each sibling is

$$\begin{aligned} H_\sigma = & \frac{m_\sigma v_r^2}{2} + \frac{m_\sigma v_z^2}{2} \\ & + \frac{\left(m_\sigma r_*^2 \dot{\phi}_* + \frac{q_\sigma}{2\pi} [\psi(r_*, z_*) - \psi(r, z)]\right)^2}{2m_\sigma r^2} \\ & - \frac{m_\sigma MG}{\sqrt{r^2 + z^2}}. \end{aligned} \quad (55)$$

Using Eq.8 we now define

$$\langle \omega_{c\sigma} \rangle = \frac{q_\sigma \langle B_z \rangle}{m_\sigma} \quad (56)$$

as the spatially-averaged cyclotron frequency over the area bounded by the poloidal field magnetic axis. We now normalize all quantities to appropriate combinations of a and Ω_0 ,

the Kepler angular frequency at a prescribed by Eq.23. The normalized time, cylindrical coordinates, velocities, and magnetic flux are thus

$$\begin{aligned}
\tau &= \Omega_0 t \\
\bar{r} &= r/a \\
\bar{z} &= z/a \\
\bar{v}_r &= v_r/a\Omega_0 \\
\bar{v}_z &= v_z/a\Omega_0 \\
\bar{L} &= L_\sigma/m_\sigma a^2 \Omega_0 \\
\bar{p}_\phi &= \bar{r}^2 d\phi/d\tau = \bar{L} \cos \theta \\
\bar{\psi}(r, z) &= \frac{\psi(r, z)}{\psi(a, 0)} = \frac{\psi(r, z)}{\langle B_z \rangle \pi a^2} \\
\bar{H} &= \frac{H}{m\Omega_0^2 a^2}
\end{aligned} \tag{57}$$

in which case Eq.55 becomes

$$\begin{aligned}
\bar{H} &= \frac{\bar{v}_r^2}{2} + \frac{\bar{v}_z^2}{2} \\
&+ \frac{\left(\bar{L} \cos \theta + \frac{\langle \omega_{c\sigma} \rangle}{2\Omega_0} [\bar{\psi}(\bar{r}_*, \bar{z}_*) - \bar{\psi}(\bar{r}, \bar{z})] \right)^2}{2 \bar{r}^2} \\
&- \frac{1}{\sqrt{\bar{r}^2 + \bar{z}^2}}.
\end{aligned} \tag{58}$$

The effective potential is now

$$\begin{aligned}
\chi(\bar{r}, \bar{z}) &= \frac{\left(\underbrace{\bar{L} \cos \theta}_{\text{mechanical}} + \underbrace{\frac{\langle \omega_{c\sigma} \rangle}{2\Omega_0} [\bar{\psi}(\bar{r}_*, \bar{z}_*) - \bar{\psi}(\bar{r}, \bar{z})]}_{\text{magnetic}} \right)^2}{2 \bar{r}^2} \\
&- \underbrace{\frac{1}{\sqrt{\bar{r}^2 + \bar{z}^2}}}_{\text{gravitational}}
\end{aligned} \tag{59}$$

where the mechanical, magnetic, and gravitational contributions have been labeled. Before photo-emission, the mechanical angular momentum is invariant so $\bar{p}_\phi(\bar{r}_*, \bar{z}_*) = \bar{L} \cos \theta$ is just the normalized mechanical angular momentum that the parent had when it was at infinity. Invoking Eq.29, it is seen that

$$0 \leq \bar{L} < \sqrt{2\bar{R}_*^2 \bar{H} + 2\bar{R}_*} \tag{60}$$

is required since incident neutral dust grains with mechanical angular momentum outside this range would have reflected at larger radii than \bar{R}_* and so would not have been able to access the radius \bar{R}_* .

The normalized canonical angular momentum with which a typical sibling charged particle is endowed is

$$\bar{P}_\phi = \bar{L} \cos \theta + \frac{\langle \omega_{c\sigma} \rangle}{2\Omega_0} \bar{\psi}(\bar{r}_*, \bar{z}_*). \quad (61)$$

The parameters underlying Fig.3(b) can now be understood. This figure is a plot of $\chi(\bar{r}, \bar{z})$ v. \bar{r} for $\bar{z} = 0$ where \bar{P}_ϕ is calculated for the situation where $\langle \omega_{c\sigma} \rangle / \Omega_0 = 40$, $\bar{r}_* = 0.5$, $\bar{z}_* = 0$, $\theta = 0$, and $\bar{L} = 1$. Charging of an $\bar{L} = 1$ dust grain via photo-emission causes the effective potential governing the dust grain to change from the form given in Fig.3(a) to the form given in Fig.3(b).

When the magnetic term in Eq.59 becomes comparable to the mechanical term or much larger, orbital dynamics for the siblings become very different from the orbital dynamics of the neutral parent that existed before photo-emission. Various orbits can occur for the siblings. Because of the complexity of these three dimensional orbits, we will first consider orbits confined to the $\bar{z} = 0$ plane and then generalize to fully three dimensional orbits ranging over finite \bar{z} .

6.2. Distribution of Cometary, Speiser, Cyclotron, and Drain-Hole Orbits

As reviewed in Sec.4, neutral particles orbits are degenerate with respect to their orbital plane inclination angle θ (see Fig.2). However, once particles become charged, they are no longer restricted to an orbital plane, and furthermore, as seen from Eq.59, the effective potential of a charged particle has a strong dependence on the value of θ that its parent particle had. This dependence was manifested in the discussion of Fig. 4 where it was noted that particles with $|2\pi P_\phi / q_\sigma \psi_0| \gg 1$ are essentially unmagnetized and have Keplerian cometary orbits, particles with $2\pi P_\phi \theta / q_\sigma \psi_0 \simeq 1$ have Speiser orbits, particles with $0 \ll 2\pi P_\phi / q_\sigma \psi_0 \ll 1$ have cyclotron orbits, and particles with $2\pi P_\phi / q_\sigma \psi_0 \simeq 0$ have drain-hole orbits. This discussion can be made more quantitative by defining $\Lambda \equiv 2\pi P_\phi / q_\sigma \psi_0$; note that Λ corresponds to the horizontal dashed lines in the left hand column of Fig.4. Equation 61 can then be recast as

$$\Lambda = \frac{2\Omega_0}{\langle \omega_{c\sigma} \rangle} \bar{L} \cos \theta + \bar{\psi}(\bar{r}_*, \bar{z}_*). \quad (62)$$

Thus particles with $|\Lambda| \gg 1$ have Keplerian cometary orbits, particles with $\Lambda \simeq 1$ have Speiser orbits, particles with $0 \ll \Lambda \ll 1$ have cyclotron orbits, and particles with $\Lambda \simeq 0$ have drain-hole orbits.

Assuming $\bar{H} \ll 1$ and $\bar{R}_* \sim 1$, Eq.60 implies that only particles with $0 < \bar{L} < \sqrt{2}$ can access a given location. Because there will be a distribution of all possible \bar{L} 's within this allowed range, we consider a particle with the mean of these allowed values as being

representative and so assume that $\bar{L} = \sqrt{2}/2$ is the normalized angular momentum of this representative nominal particle.

Since $\langle \omega_{c\sigma} \rangle = q_\sigma \langle B_z \rangle / m_\sigma$, $\langle B_z \rangle = \psi_0 / \pi a^2$, and $\Omega_0 = \sqrt{MG/a^3}$ this nominal particle will have

$$\Lambda = K \cos \theta + \bar{\psi}(\bar{r}_*, \bar{z}_*) \quad (63)$$

where

$$K = \frac{m_\sigma}{q_\sigma} \frac{\pi \sqrt{2aMG}}{\psi_0} \quad (64)$$

parameterizes the competition between gravitational and magnetic forces. Using Eq. 46 to give the charge to mass ratio it is seen that

$$K = \frac{\pi \rho_d^{int} \sqrt{2aMG}}{3\varepsilon_0 (W_{photon} - W_{wf}) \psi_0} r_d^2; \quad (65)$$

thus K increases when r_d increases as a result of dust grain coagulation.

Speiser and drain hole particles occur when gravitational and magnetic forces are comparable in magnitude, i.e., when K is of order unity. For a given star mass M , poloidal flux magnetic axis radius a , and magnetic flux ψ_0 , this means that Speiser and drain hole particles will occur when coagulation has caused the dust grains to have a certain critical radius which is of order

$$r_d^{crit} \sim \frac{1}{(2aMG)^{1/4}} \sqrt{\frac{3\varepsilon_0 (W_{photon} - W_{wf}) \psi_0}{\pi \rho_d^{int}}}. \quad (66)$$

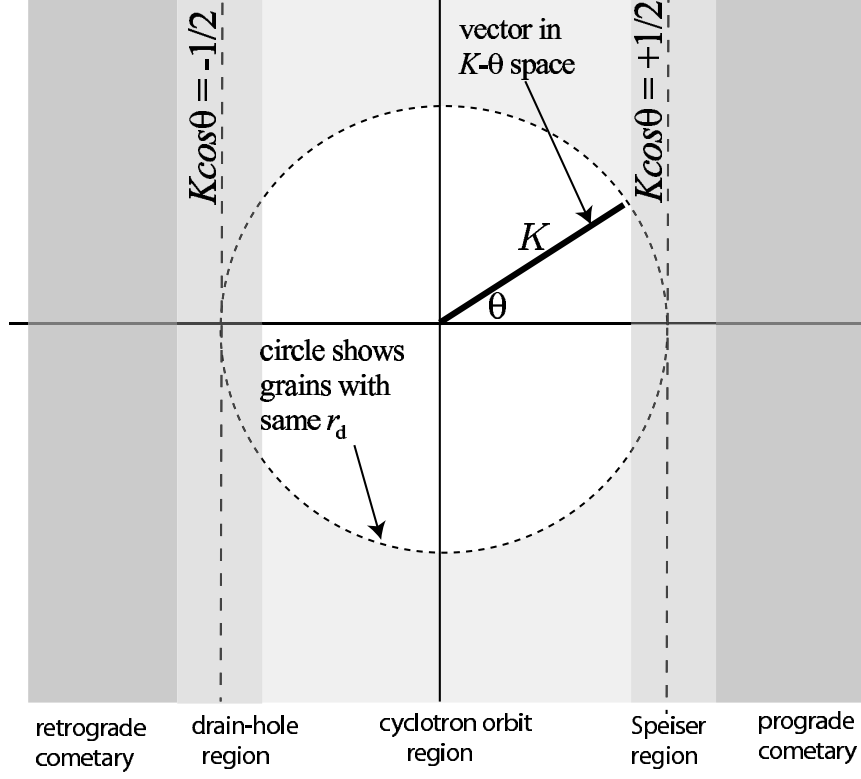
If $r_d \gg r_d^{crit}$ then gravity will dominate and the dust grains will behave like neutral particles whereas if $r_d \ll r_d^{crit}$ then magnetic forces will dominate and charged dust grains will mainly have cyclotron orbits. Since coagulation causes r_d to increase monotonically, there should always be some time when $r_d \sim r_d^{crit}$ and K is of order unity. This argument indicates that the dust-driven dynamo mechanism should take place as a well-defined temporal stage in the accretion process; before this stage r_d is too small and after this stage r_d is too large.

Since $\bar{\psi}(\bar{r}_*, \bar{z}_*)$ ranges between 0 and 1, let us consider the nominal situation where $\bar{\psi}(\bar{r}_*, \bar{z}_*) = 1/2$ in which case

$$\Lambda_{nom} = K \cos \theta + \frac{1}{2}. \quad (67)$$

If $K \simeq 1/2$, Speiser particles result for $\cos \theta = 1$ (i.e., neutral parent was prograde) and drain-hole particles result for $\cos \theta = -1$ (i.e., neutral parent was retrograde). If $K \ll 1/2$, the orbits will be cyclotron. Finally if $K \gg 1/2$, the orbits will be cometary if $\cos \theta$ is not close to zero. The categorization implied by Eq.67 is shown schematically in Fig. 5.

Fig. 5.— Distribution of orbits as function of K, θ . Radius K is proportional to r_d^2 . Prograde orbits have $\theta = 0$, retrograde orbits have $\theta = \pi$, and polar orbits have $|\theta| = \pi/2$.



6.3. Light-weight particles ($K \ll 1$)

6.3.1. Generic accretion mechanism

Potential barriers occur at locations where $\chi(\bar{r}, \bar{z}) > \bar{H}$. We first consider motion of a sibling particle constrained to stay in the $\bar{z} = 0$ plane (i.e., the particle starts with $\bar{v}_z = 0$ and no forces exist that push it off the $\bar{z} = 0$ plane). In this case the effective potential is a function of \bar{r} only and is

$$\chi(\bar{r}, 0) = \frac{\left(\underbrace{\bar{L} \cos \theta}_{\text{mechanical}} + \underbrace{\frac{\langle \omega_{c\sigma} \rangle}{2\Omega_0} [\bar{\psi}(\bar{r}_*, 0) - \bar{\psi}(\bar{r}, 0)]}_{\text{magnetic}} \right)^2}{2\bar{r}^2} - \underbrace{\frac{1}{\bar{r}}}_{\text{gravitational}}. \quad (68)$$

If $\chi(\bar{r}, 0)$ exceeds \bar{H} at some radius $\bar{r} > \bar{r}_*$, the particle becomes trapped within a finite extent region as indicated in Fig.3(b) or equivalently by the third and fourth rows, right hand column of Fig. 4. If \bar{r}_* is small or large compared to unity so r_* is not near the peak of $\bar{\psi}$, then $\bar{\psi}(\bar{r}_*, 0) \ll 1$. Because the particle is assumed to be light-weight (i.e., $r_d \ll r_d^{crit}$), its average-field cyclotron frequency $\langle \omega_{c\sigma} \rangle$ will be much larger than the Kepler frequency Ω_0 . Since \bar{L} is of order unity, the light-weight particle will have $|\langle \omega_{c\sigma} \rangle / 2\Omega_0| \gg \bar{L}$ in which case

$$\max \left\{ \frac{\left(\bar{L} \cos \theta + \frac{\langle \omega_{c\sigma} \rangle}{2\Omega_0} [\bar{\psi}(\bar{r}_*, 0) - \bar{\psi}(\bar{r}, 0)] \right)^2}{2\bar{r}^2} \right\} \simeq \max \left\{ \frac{1}{2\bar{r}^2} \left(\frac{\langle \omega_{c\sigma} \rangle}{2\Omega_0} \bar{\psi}(\bar{r}, 0) \right)^2 \right\}$$

so the peak of $\chi(\bar{r}, 0)$ will occur where $\bar{\psi}(\bar{r}, 0)$ takes on its maximum value, namely unity. The maximum of $\chi(\bar{r}, 0)$ for a light-weight particle is thus

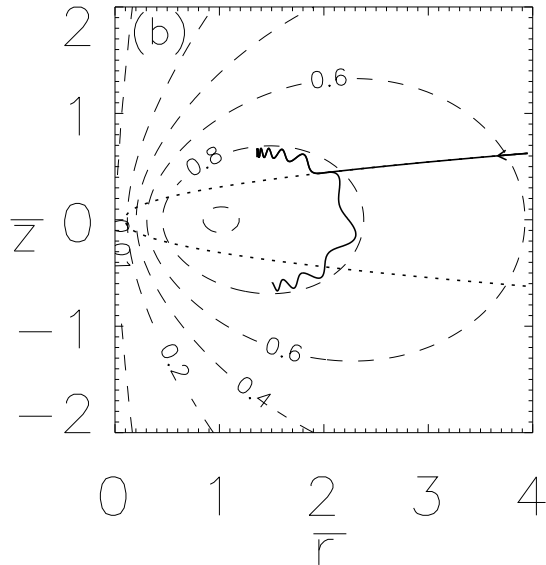
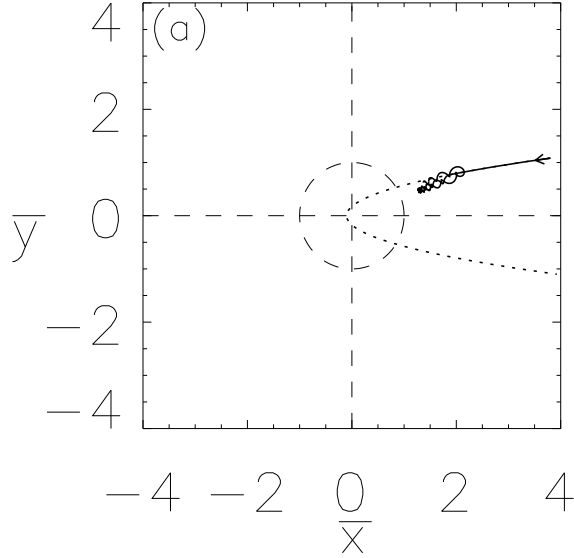
$$\chi(1, 0) \simeq \frac{1}{2} \left(\frac{\langle \omega_{c\sigma} \rangle}{2\Omega_0} \right)^2 - 1 \quad (69)$$

where the -1 term comes from the gravitational potential at $\bar{r} = 1, z = 0$. This gives the necessary condition for trapping light-weight charged dust grains to be

$$\frac{|\langle \omega_{c\sigma} \rangle|}{\Omega_0} > 2\sqrt{2}. \quad (70)$$

Because a typical light-weight grain has $|\langle \omega_{c\sigma} \rangle| \gg 2\sqrt{2}\Omega_0$, a light-weight grain confined to the $z = 0$ plane will become trapped in a finite-sized region upon being charged, i.e., it will have accreted. The same will be true for the associated sibling photo-electrons since they

Fig. 6.— An incident neutral particle ($\bar{H} = 0$, $\bar{\rho}_{pericenter} = 0.1$, $\theta = 30^\circ$, $\alpha = 0^\circ$) becomes charged due to photoemission of electrons at $R_* = 2$. The child particle mass is such that $\langle \omega_{c\sigma} \rangle / \Omega_0 = 200$ and the child particle becomes magnetically trapped, staying within a poloidal Larmor orbit of a constant ψ surface. In this example, the child particle is mirror trapped and so cannot enter the strong magnetic field region at small \bar{r} . (a) $\bar{x} - \bar{y}$ plane, charging occurs where orbit abruptly changes, poloidal field magnetic axis shown as dashed circle (b) $\bar{r} - \bar{z}$ plane showing magnetic mirroring of child particle at large magnetic field (poloidal flux contours $\bar{\psi}(\bar{r}, \bar{z})$ shown as dashed lines). The orbit the parent neutral particle would have continued to have if it had not become charged is shown by dotted line (both projections).



also have $|\langle\omega_{ce}\rangle| \gg 2\sqrt{2}\Omega_0$. Figure 6 shows a direct numerical integration of the equation of motion demonstrating this basic accretion mechanism in three dimensions: a light-weight neutral dust grain disintegrates at a certain location into an $|\langle\omega_{c\sigma}\rangle| \gg 2\sqrt{2}\Omega_0$ positively charged dust grain (there would also be Z associated photo-electrons which for clarity are not shown in the figure but would also have cyclotron-type orbits). An actual dust grain would start with an infinitesimal energy $0 < \bar{H} \ll 1$; the calculation here uses $\bar{H} = 0$ as representative of this infinitesimal \bar{H} since the difference between an orbit with $\bar{H} = 0$ and an orbit with infinitesimal \bar{H} is insignificant at any finite distance. The newly created charged particles are trapped to the vicinity of a $\bar{\psi}(\bar{r}, \bar{z}) = \text{const.}$ poloidal flux surface (poloidal flux surfaces are shown by dashed lines in Fig.6(b)). Because of μ conservation, the charged particles can also be mirror-trapped, so while on the the constant $\bar{\psi}$ surface, they reflect from regions of this surface where the magnetic field is strong. Figure 7(a) plots the time dependence of \bar{p}_ϕ for the particle shown in Fig.6.

Figure 7(b) plots the canonical angular momentum \bar{P}_ϕ (solid line) and the kinetic/potential energies (dashed lines labeled ‘KE’ and ‘PE’ in figure). It is seen that \bar{p}_ϕ is conserved before charging whereas \bar{P}_ϕ is the conserved quantity after charging. Also, the total energy (kinetic + potential, dashed line labeled ‘Tot’ in figure) remains zero. Strictly speaking, this plot should be considered as referring to the neutral dust grain until charging, and then to the charged dust grain after charging so the jump in \bar{P}_ϕ at the charging time seen in the figure does not violate the requirement that \bar{P}_ϕ is a constant of the motion for a specific particle.

Figure 8 shows the three dimensional orbit of a light-weight charged dust grain with slightly different parameters so that it is not mirror trapped. The derivation of the non-dimensional equation of motion used here is given in Appendix D.

6.3.2. Width of light-weight particle trapping well and relation to cyclotron orbits

If $|\langle\omega_{c\sigma}\rangle|/2\Omega_0 \gg |\bar{p}_\phi(\bar{r}_*, \bar{z}_*)|$, the magnetic term in Eq.59 dominates the mechanical term as soon as \bar{r} deviates slightly from r_* . This implies existence of a narrow trench-like potential well with minimum very close to r_* . The effective potential shown Fig.3(b) has such a trench; this situation involves a particle confined to the $\bar{z} = 0$ plane and the trench is at $\bar{r} = \bar{\rho} = 0.55$. This situation is also evident in the third and fourth rows, right hand column of Fig. 4. If $|\langle\omega_{c\sigma}\rangle| \gg \Omega_0$ the gravitational term is completely overwhelmed by the magnetic term so the trench bottom in the $z = 0$ plane is where

$$\bar{\psi}(\bar{r}) = \frac{\Omega_0}{\langle\omega_{c\sigma}\rangle} \bar{p}_\phi(\bar{r}_*, \bar{z}_*) + \bar{\psi}(r_*). \quad (71)$$

Fig. 7.— (a) Mechanical angular momentum \bar{p}_ϕ v. time τ and (b) kinetic energy (KE), potential energy (PE) and canonical angular momentum \bar{P}_ϕ v. time for the calculation shown in Fig. 6. Mechanical angular momentum \bar{p}_ϕ is conserved before charging, but oscillates after charging; canonical angular momentum \bar{P}_ϕ is much larger than mechanical angular momentum because of strong magnetic field and is conserved after charging.

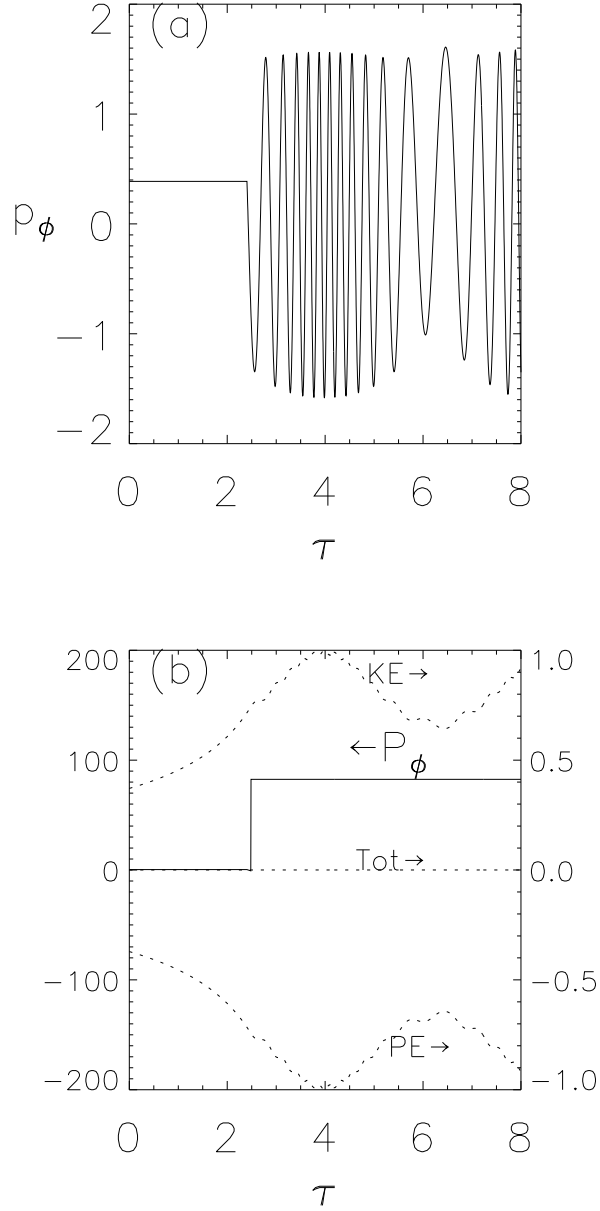
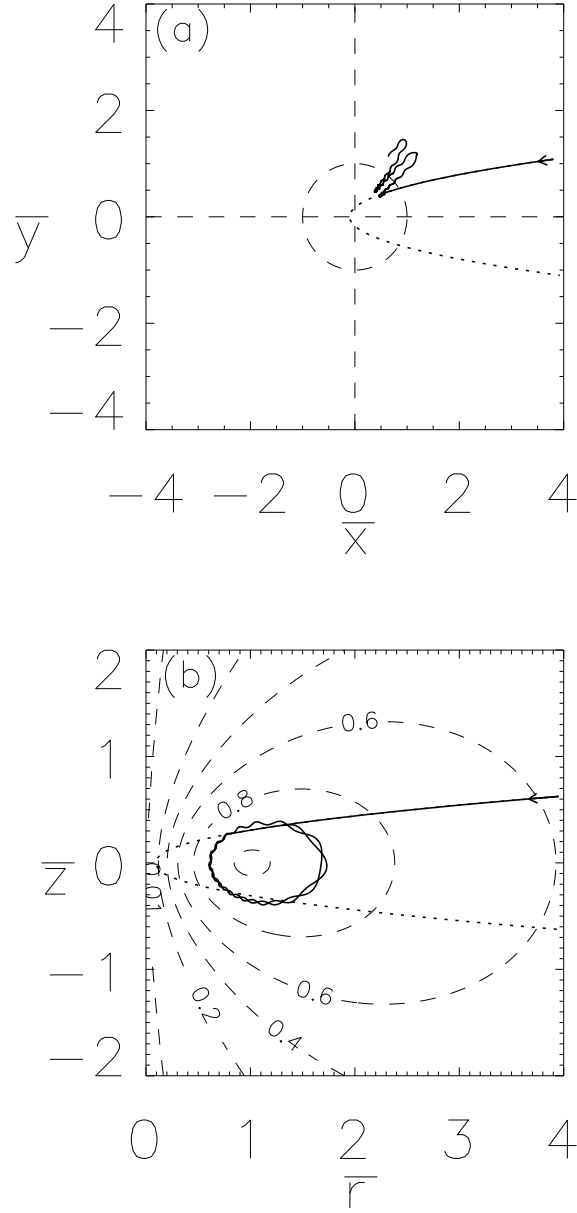


Fig. 8.— Same parameters as Fig. 6, except $R_* = 0.8$. Charged particle is now not mirror-trapped.



Taylor expansion of $\bar{\psi}(\bar{r})$ near r_* gives

$$\begin{aligned}\bar{\psi}(\bar{r}) = & \bar{\psi}(\bar{r}_*) + (\bar{r} - \bar{r}_*) \left(\frac{\partial \bar{\psi}}{\partial \bar{r}} \right)_{\bar{r}=\bar{r}_*} \\ & + \frac{1}{2} (\bar{r} - \bar{r}_*)^2 \left(\frac{\partial^2 \bar{\psi}}{\partial \bar{r}^2} \right)_{\bar{r}=\bar{r}_*} + \dots\end{aligned}\quad (72)$$

If \bar{r}_* is not close to unity, then $\bar{\psi}(\bar{r}_*)$ is not close to its maximum value so the leading term in the Taylor expansion is the one involving $\partial \bar{\psi} / \partial \bar{r}$. Using Eq.72 to substitute for $\bar{\psi}(\bar{r})$ in Eq.71 gives the trench bottom to be at

$$\bar{r} = \bar{r}_* + \frac{2}{\left(\partial \bar{\psi} / \partial \bar{r} \right)_{\bar{r}=\bar{r}_*}} \frac{\Omega_0}{\langle \omega_{c\sigma} \rangle} \bar{p}_\phi(\bar{r}_*, \bar{z}_*) \quad (73)$$

so the trench bottom is close to \bar{r}_* because $|\langle \omega_{c\sigma} \rangle| \gg \Omega_0$ is being assumed. If $\bar{r}_* < 1$ then $(\partial \bar{\psi} / \partial \bar{r})_{\bar{r}=\bar{r}_*}$ is positive and vice versa since $\bar{\psi}$ has its maximum value at $\bar{r} = 1$. The trench bottom will thus be outside of \bar{r}_* if $\bar{r}_* < 1$ so $\langle \omega_{c\sigma} \rangle (\partial \bar{\psi} / \partial \bar{r})_{\bar{r}=\bar{r}_*}$ is positive and vice versa if $\bar{r}_* > 1$. The sign of $\bar{\psi}(\bar{r}) - \bar{\psi}(\bar{r}_*)$ oscillates as the particle bounces back and forth in the trench. Using Eq.41 expressed in normalized variables, and noting that $\bar{P}_\phi = \bar{p}_\phi(\bar{r}_*, \bar{z}_*) + \bar{\psi}(\bar{r}_*, \bar{z}_*) \langle \omega_{c\sigma} \rangle / 2\Omega_0$ it is seen that the azimuthal velocity

$$\begin{aligned}\frac{d\phi}{d\tau} &= \frac{\bar{P}_\phi - \frac{\langle \omega_{c\sigma} \rangle}{2\Omega_0} \bar{\psi}(\bar{r})}{\bar{r}^2} \\ &= \frac{\bar{p}_\phi(\bar{r}_*, \bar{z}_*) - \frac{\langle \omega_{c\sigma} \rangle}{2\Omega_0} [\bar{\psi}(\bar{r}) - \bar{\psi}(\bar{r}_*)]}{\bar{r}^2}\end{aligned}\quad (74)$$

has an oscillating polarity. The combined oscillation of \bar{r} and $d\phi/d\tau$ corresponds to the particle tracing out Larmor orbits with gyro-center at the trench bottom (Schmidt 1979).

To summarize: In the $|\langle \omega_{c\sigma} \rangle| / \Omega_0 \gg 1$ situation (i.e., light-weight particles) Eq. 59 provides an effective potential whereby the magnetized charged particle is confined to the vicinity of a constant ψ surface, just like a charged particle in a tokamak (Rome & Peng 1979). The particle motion over the constant ψ surface can be understood as a sum of parallel to \mathbf{B} motion, cyclotron motion, and particle drifts (curvature, grad B , etc.) as given by Eq.C5. Furthermore, regions where μB is large can constitute an additional potential barrier (i.e., magnetic mirror) that prevents those subsets of particles having inadequate velocity parallel to \mathbf{B} from accessing the entire constant ψ surface. Because of magnetic mirroring by $\mu \nabla B$ forces, particles in these subsets are confined to the weaker magnetic field regions of a constant ψ surface as seen in Fig.6(b).

6.4. Speiser orbit particles ($K \cos \theta \simeq 1/2$)

When $\bar{r}_* \simeq 1$ and $\bar{z}_* \simeq 0$, photoemission occurs near the peak of $\psi(\bar{r}, \bar{z})$, i.e., where $\nabla \psi \simeq 0$; see Fig. 4 second row from top where P_ϕ is just grazing the peak of ψ . The linear term

in the Taylor expansion in Eq.72 is therefore negligible. Since $\partial^2 \bar{\psi} / \partial \bar{r}^2$ is negative near the maximum of $\bar{\psi}$, Eq.72 becomes

$$\bar{\psi}(\bar{r}) \simeq \bar{\psi}(\bar{r}_*) - \frac{1}{2} (\bar{r} - \bar{r}_*)^2 \left| \left(\frac{\partial^2 \bar{\psi}}{\partial \bar{r}^2} \right)_{\bar{r}=\bar{r}_*} \right|. \quad (75)$$

Equation 74 then reduces to

$$\frac{d\phi}{d\tau} = \frac{\bar{p}_\phi(\bar{r}_*, 0) + \frac{\langle \omega_{c\sigma} \rangle}{4\Omega_0} (\bar{r} - \bar{r}_*)^2 \left| \left(\frac{\partial^2 \bar{\psi}}{\partial \bar{r}^2} \right)_{\bar{r}=\bar{r}_*} \right|}{\bar{r}^2} \quad (76)$$

and for $\bar{p}_\phi(\bar{r}_*, 0)$ being positive (i.e., parent particle was prograde), $d\phi/d\tau$ is always positive. This corresponds to Speiser-type orbits because when the particles bounce back and forth across the peak of ψ , they are bouncing back and forth between regions where the poloidal magnetic field $\sim \partial\psi/\partial r$ changes sign. As discussed in Section C.3 of Appendix C, this results in paramagnetism, i.e., positively charged particles moving in the positive ϕ direction and so *producing* rather than opposing a B_z field. Creation of Speiser-orbiting particles sustains the poloidal magnetic field against losses and will amplify an initial seed poloidal field; creation of Speiser particles therefore constitutes a dynamo for driving toroidal current.

Figure 9 shows the creation of a Speiser orbit by photo-emission charging of a neutral particle near the poloidal field magnetic axis. Figure 9(a) shows that the orbit is paramagnetic (i.e., particle moves in positive ϕ direction) while Fig. 9(b) shows that the orbit involves repeated reflection from the interior of a poloidal flux surface in the manner discussed in Section C.3 of Appendix C.

6.5. Drain-hole particles ($K \cos \theta \simeq -1/2$)

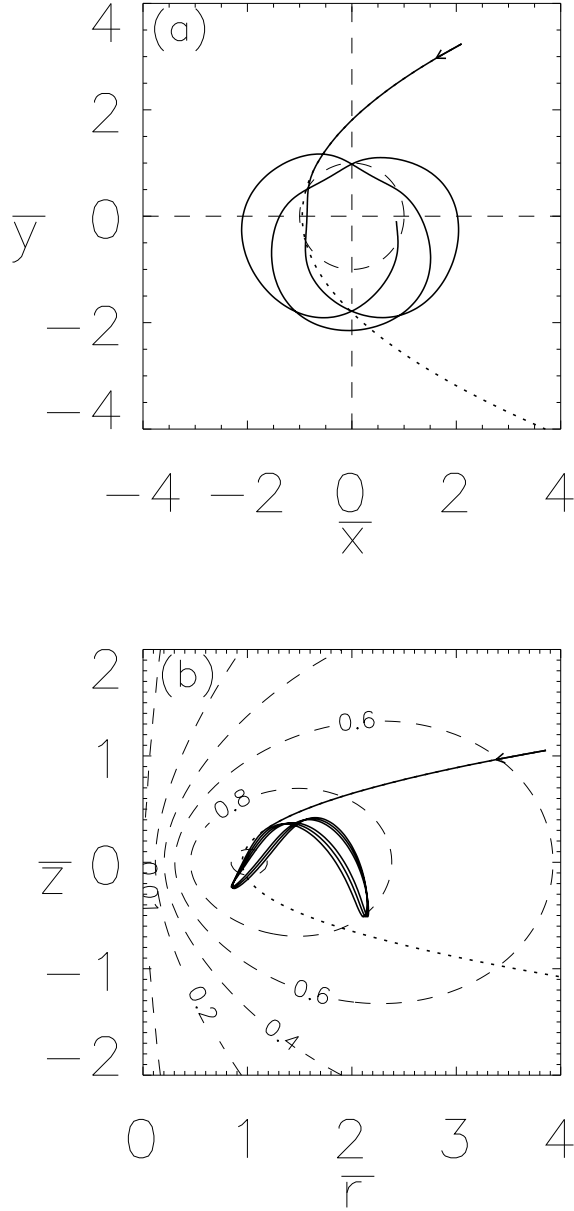
Charged particles born with $\bar{P}_\phi = 0$ are called ‘drain-hole’ particles because they behave as if they are going down a drain. The properties of drain-hole particles restricted to the $z = 0$ plane were briefly examined in Bellan (2007); here the more general 3D situation will be considered. Using Eq.61 and $\bar{p}_\phi(\bar{r}_*, \bar{z}_*) = \bar{L} \cos \theta$ the $\bar{P}_\phi = 0$ condition corresponds to

$$\bar{L} \cos \theta = -\frac{\langle \omega_{c\sigma} \rangle}{2\Omega_0} \bar{\psi}(\bar{r}_*, \bar{z}_*) \quad (77)$$

implying that $\cos \theta$ is negative in which case the parent particle must have been retrograde. The effective potential (see Eq.59) for the $\bar{P}_\phi = 0$ class of particles reduces to

$$\chi(\bar{r}, \bar{z}) \simeq \frac{\langle \omega_{c\sigma} \rangle^2}{8\Omega_0^2} \frac{(\bar{\psi}(\bar{r}, \bar{z}))^2}{\bar{r}^2} - \frac{1}{\sqrt{\bar{r}^2 + \bar{z}^2}} \quad (78)$$

Fig. 9.— Speiser orbit resulting from parent with $\bar{H} = 0$, $\bar{\rho}_{pericenter} = 0.95$, $\theta = 18^\circ$, $\alpha = 0^\circ$. Charging occurs at $\bar{R}_* = 1.2$ and the child particle is a positive particle with $\omega_{c\sigma}/\Omega_0 = 10$; (a) the \bar{x} - \bar{y} plane orbit is counter-clockwise corresponding to paramagnetic motion; (b) the \bar{r} - \bar{z} plane orbit involves the particle continuously reflecting from the interior of a toroidal flux tube.



which has a funnel (i.e., drain-like) profile near $\bar{r} = 0, \bar{z} = 0$ due to the second (gravitational) term and a hill on the funnel side wall with peak near $\bar{r} = \bar{a}, \bar{z} = 0$ due to the first (Störmer) term. A particle initially on the hill (i.e., near the poloidal field magnetic axis) will fall down the hill into the drain-like funnel; see right hand column, second row from bottom in Fig. 4 for plot of first term in Eq.78. Thus, no matter where a $\bar{P}_\phi = 0$ particle starts in \bar{r}, \bar{z} space, it eventually follows a spiral path down to $\bar{r} = 0, \bar{z} = 0$; no centrifugal force will ever push it back outwards because the first term in Eq.78 has no singularity at $\bar{r} = 0$ (recall that $\bar{\psi} \sim \bar{r}^2$ for small \bar{r}, \bar{z}). The sense of this downward spiraling trajectory will be in the $-\langle\omega_{c\sigma}\rangle$ direction as shown by Eq.74. Since $\bar{\psi} \sim \bar{r}^2$ for small \bar{r}, \bar{z} it is seen from Eq.74 that drain-hole particles have a limiting angular velocity

$$\lim_{\bar{r}, \bar{z} \rightarrow 0} \frac{d\phi}{d\tau} = - \frac{\langle\omega_{c\sigma}\rangle}{2\Omega_0} \lim_{\bar{r}, \bar{z} \rightarrow 0} \left(\frac{\bar{\psi}(\bar{r}, \bar{z})}{\bar{r}^2} \right) = \text{const.} \quad (79)$$

Combination of Eqs. 29 and 77 show that drain-hole particles can only be created if the accessibility condition

$$\frac{\langle\omega_{c\sigma}\rangle^2}{4\Omega_0^2} (\bar{\psi}(\bar{r}_*, \bar{z}_*))^2 < (2\bar{\rho}^2 \bar{H} + 2\bar{\rho}) \cos^2 \theta \quad (80)$$

is satisfied, a condition that $\langle\omega_{c\sigma}\rangle/\Omega_0$ not be too large. Since $\bar{H} \simeq 0$ is assumed, $\cos \theta \simeq -1$ for drain-hole particles, and since $\bar{\rho} = \sqrt{\bar{r}^2 + \bar{z}^2}$ is required to be larger than the pericenter, this condition becomes

$$|\bar{\psi}(\bar{r}_*, \bar{z}_*)| < \left| \frac{2\Omega_0}{\langle\omega_{c\sigma}\rangle} \sqrt{2\bar{\rho}_{\text{pericenter}}} \right|. \quad (81)$$

Because Eq.81 requires $\langle\omega_{c\sigma}\rangle/\Omega_0$ to be small, drain-hole particles, like Speiser particles, result from dust grains with grain radii consistent in order of magnitude with Eq.66.

Particles with \bar{P}_ϕ exactly zero (“perfect” drain-hole particles) fall down the gravitational potential all the way to the central object at the origin $\bar{r} = 0, \bar{z} = 0$. Particles that are not quite perfect drain-hole particles will have small, but finite \bar{P}_ϕ and so will reflect when close to the central object.

Figure 10 shows a numerical calculation of a drain-hole particle orbit with $\bar{H} = 0$. The solid line in Fig. 10(a) shows the projection of the drain-hole orbit in the \bar{x} - \bar{y} plane. The orbit the neutral particle would have had if it had not encountered any photons and so remained neutral is shown as a dotted line. Figure 10(b) shows the projection in the \bar{r} - \bar{z} plane with surfaces of constant $\bar{\psi}$ indicated (the dotted line again shows the orbit the neutral particle would have had if it had not encountered any photons). The drain-hole particle has a retrograde orbit (clockwise sense resulting from its angle of inclination $\theta > 90^\circ$). Figure 11(a) shows that the mechanical angular momentum is not constant after charging while Fig.

Fig. 10.— Drain-hole particle ($\bar{H} = 0$, $\bar{\rho}_{pericenter} = 0.2$, $\theta = 170^\circ$, $\alpha = 0$, $\bar{R}_* = 0.8$) falls across magnetic field all the way to the central object. This is a heavy particle (dust grain) and has $\omega_{c\sigma}/\Omega_0 = 1.6$; (a) shows orbit projection in \bar{x} - \bar{y} plane, (b) shows projection in \bar{r} - \bar{z} plane. Dotted line shows trajectory parent would have continued to have if it had not become charged.

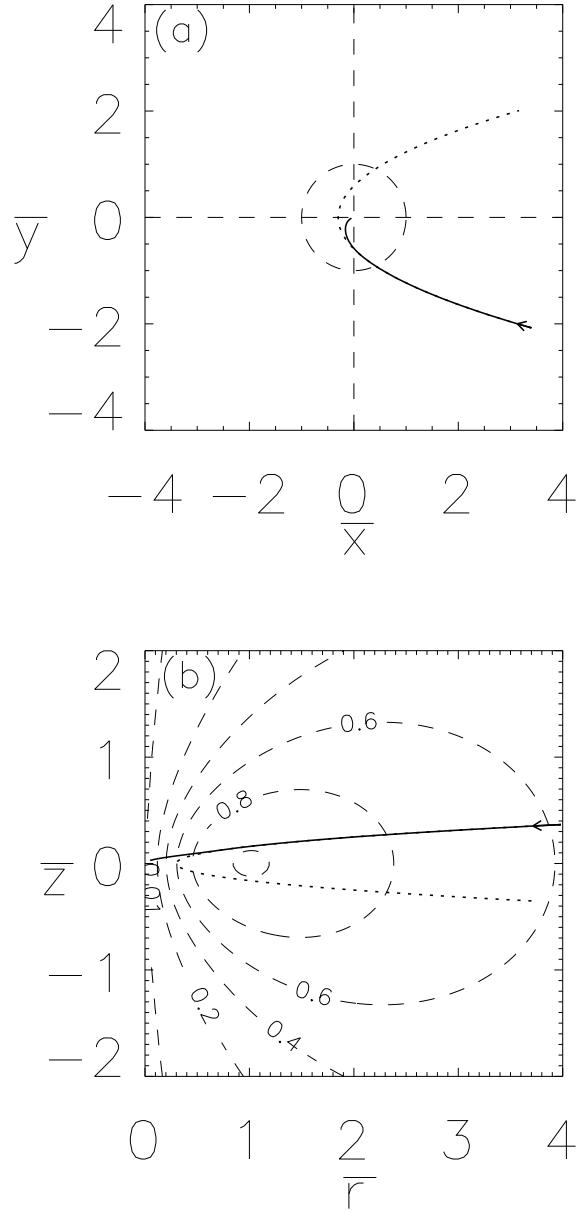
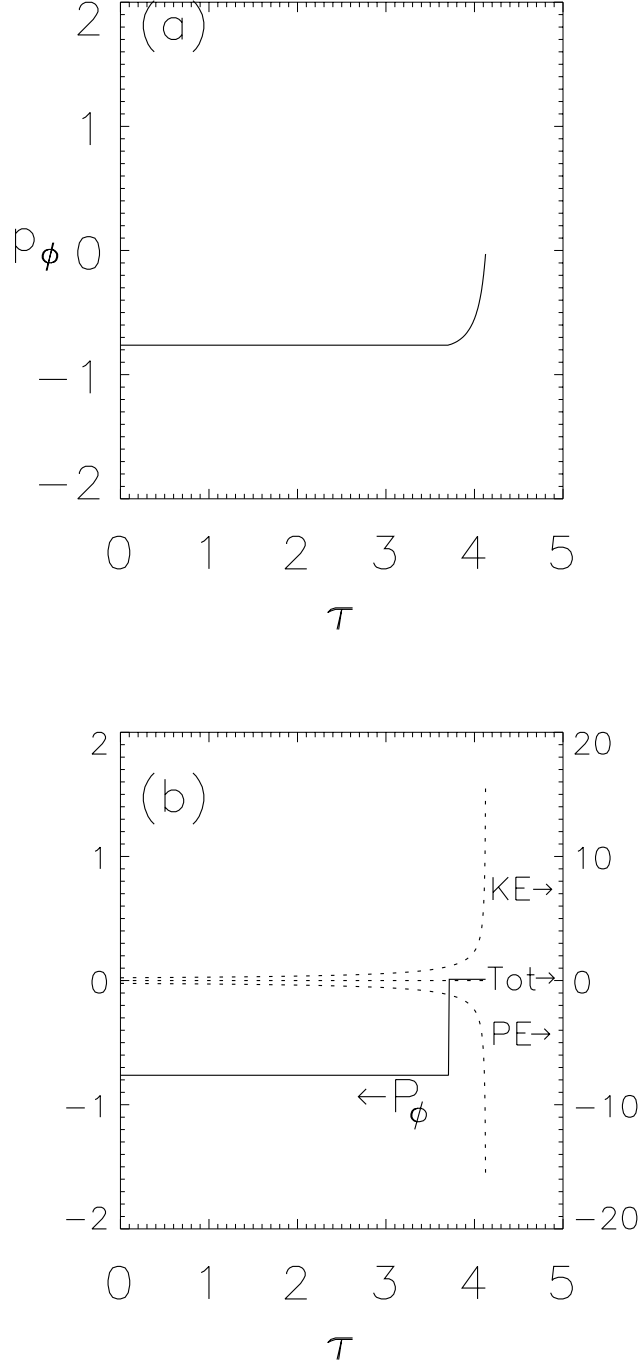


Fig. 11.— (a) Mechanical angular momentum p_ϕ for drain-hole particle is not conserved when particle becomes charged, (b) canonical angular momentum P_ϕ , kinetic energy (KE) and potential energy (PE). The magnitudes of the kinetic and potential energy increase without bound as the particle falls towards the central object. The canonical angular momentum is conserved and is near zero upon charging.



11(b) shows that the canonical angular momentum remains constant at zero after charging. Figure 11(b) also shows how the magnitudes of the potential and kinetic energies increase without bound as the particle descends towards the central object while the total energy stays zero (kinetic, potential and total energies shown as dashed lines).

When drain-hole particles approach the central object, the gravitational term in Eq.78 dominates (recall that $\bar{\psi} \sim \bar{r}^2$ at small \bar{r} and near $\bar{z} = 0$). It therefore makes sense to use spherical coordinates in this region in which case the Hamiltonian is approximately

$$0 \simeq \frac{1}{2} \left(\frac{d\bar{R}}{d\tau} \right)^2 - \frac{1}{\bar{R}} \quad (82)$$

where \bar{R} is the spherical radius and $\bar{H} \simeq 0$ has been assumed. Equation 82 shows that the free-fall velocity scales as

$$\left| \frac{d\bar{R}}{d\tau} \right| = \sqrt{\frac{2}{\bar{R}}} \quad (83)$$

and particle flux conservation over a spherical surface $4\pi\bar{R}^2$ shows that $4\pi\bar{R}^2 n_{dh}(\bar{R}) d\bar{R}/d\tau = \text{const.}$ where $n_{dh}(\bar{R})$ is the density of drain-hole particles. Thus, if the incoming drain-hole particles do not accumulate, spherical focusing combined with the accelerating free-fall velocity shows that the density of drain-hole particles scales as

$$n_{dh}(\bar{R}) \sim \frac{1}{\bar{R}^2 d\bar{R}/d\tau} \sim \frac{1}{\bar{R}^{3/2}}. \quad (84)$$

Accumulation of the drain-hole particles in the vicinity of the central object will also increase the density of drain-hole particles with time. There is thus both a temporal increase and a geometrically-induced increase of the drain-hole particle density as \bar{R} decreases. Since the sibling electrons were left stranded at large \bar{r} , what results is the establishment of a large positive charge density near the central object and an equal-magnitude negative charge density at large \bar{r} . The flow pattern of the drain hole particles and the location of the stranded electrons is sketched in Fig.12. Eventually the positive space charge near the central object becomes so large that it produces a repulsive electrostatic electric field that balances the gravitational force acting on any additional drain hole particles. The large positive potential near $\bar{r} = 0$ will tend to drive axial electric currents flowing away from the $\bar{z} = 0$ plane resulting in the loss or neutralization of some of the drain-hole particles. The axial electric current could result from attraction of electrons near $\bar{r} = 0$ towards the $\bar{z} = 0$ plane or from expulsion of positive particles away from the $\bar{z} = 0$ plane. Either electron attraction or positive particle repulsion will deplete the positive space charge density near $\bar{r} = 0$. There will then have to be a replenishing flow of additional drain hole particles into the $\bar{r} = 0$ region to compensate for this depletion of positive space charge. Being very low mass,

the stranded electrons have very small Larmor orbit radius and so are constrained to stay essentially right on the poloidal flux surface on which they were photo-emitted (see Secs.6.3 and 6.3.2). The electron flow is thus at a much larger $|\bar{z}|$ than the drain-hole particle radially inward flow which is concentrated near the $\bar{z} = 0$ plane. The vertical separation between the respective radially inward flows of positive and negative particles means that bipolar toroidal magnetic fields will be generated in the interstitial regions between the electron flow and the drain-hole flow (see positive and negative B_ϕ regions in Fig.12).

If no electric current is allowed to flow, the situation is like a free-standing battery not connected to any load, i.e., a situation where there is a voltage differential across the battery terminals, but no current flows. However, if bipolar axial currents are allowed to flow, then the situation is like a battery connected to a load and the resulting radially inward drain-hole particle current in the $\bar{z} = 0$ plane is like the internal current in a battery. The overall current flow pattern sketched in Fig.12 results from a combination of drain hole particle and electron motion. This pattern is sketched in Fig.13 as a conventional electric current. The geometry of the current flow pattern and electromotive force driving this current is identical to the geometry and flow patterns in the laboratory configuration simulating astrophysical jets described in Hsu & Bellan (2002, 2005) and Bellan *et al.* (2005). The electric field due to the drain hole particles corresponds to the electric field produced by the capacitor bank used in the laboratory experiment. This geometry and symmetry is also identical to that proposed by Lovelace (1976), the only difference being the means by which the radial electric field is produced. The magnetic fields in the lab and astrophysical plasmas have the same toroidal/poloidal topology.

The drain-hole current is thus powered by gravity and has J_r radially inward with E_r radially outward so that $\mathbf{J} \cdot \mathbf{E}$ is negative, consistent with the condition for a dynamo. The drain-hole particles have retrograde motion so their mechanical angular momentum is negative. This negative mechanical angular momentum is removed by the braking torque $\mathbf{r} \times \mathbf{F} = (r\hat{r}) \times (J_r\hat{r} \times B_z\hat{z}) = -rJ_rB_z\hat{z}$ which is positive since J_r is negative and B_z is positive.

The radially inward current is symmetric with respect to z . This property provides enough information to determine the symmetry properties of $I(r, z)$. The radially inward drain-hole current means that $J_r < 0$ and $J_z = 0$ in the $z = 0$ plane. Since Eq.5 shows that $J_r = -(2\pi r)^{-1}\partial I/\partial z$ and $J_z = (2\pi r)^{-1}\partial I/\partial r$ the condition $J_z = 0$ means $I(r, z)$ must vanish in the $z = 0$ plane. Furthermore I must be an odd function of z in order for $J_r = -(2\pi r)^{-1}\partial I/\partial z$ to be finite in the $z = 0$ plane. Finally $\partial I/\partial z$ should be positive in order to have $J_r < 0$. Thus, $I(r, z)$ should be positive for $z > 0$ and negative for $z < 0$ so that, as sketched in Fig.13, there will be a bipolar axial current flowing along the z axis outwards

Fig. 12.— Drain hole dust grains fall across poloidal field lines towards central object leaving behind stranded electrons which are confined to poloidal flux surface on which they are born. Drain hole particles accumulate near central object creating large positive charge there. This repels positive particles (drain hole particles, ions) to flow axially away from $z = 0$ plane and also attracts stranded electrons which can flow on poloidal flux surface. The result is a clockwise poloidal current flow pattern in upper-half r - z plane, giving a positive B_ϕ in region linked by poloidal current and a negative B_ϕ in lower-half r - z plane where poloidal current flow is counter-clockwise.

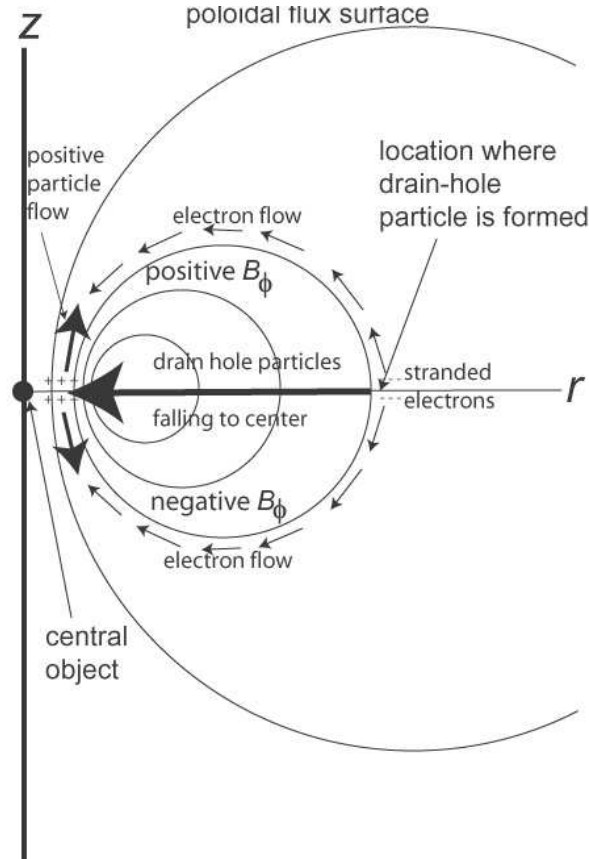
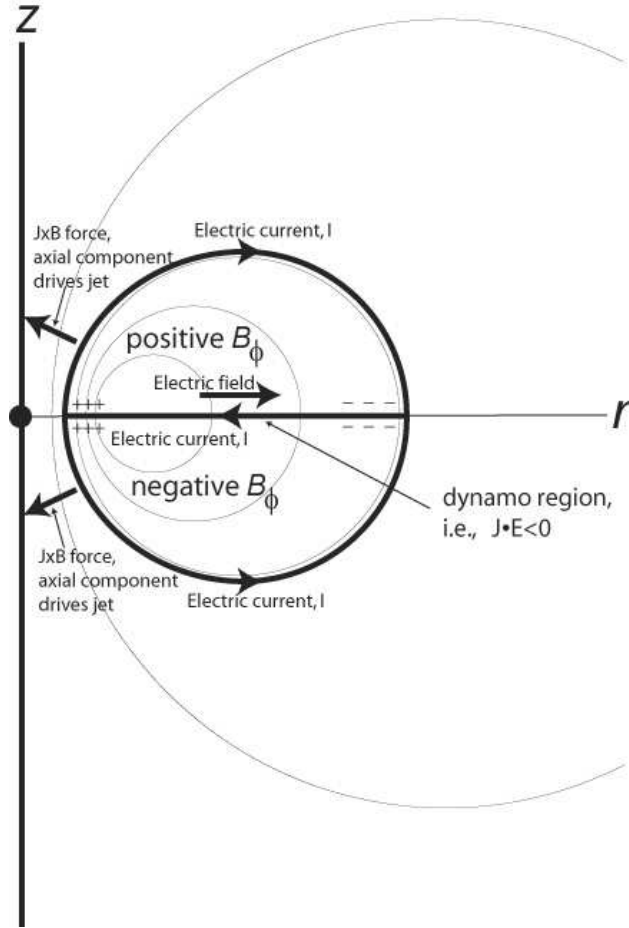


Fig. 13.— Flow of conventional electric current for drain hole particles and their associated stranded electrons. The electric field on the $z = 0$ plane is radially outwards while the current flow is radially inwards so $\mathbf{J} \cdot \mathbf{E}$ is negative, indicating that the infall of the drain-hole particles constitutes a dynamo. The $\mathbf{J} \times \mathbf{B}$ force (which is essentially due to the gradient of B_ϕ^2 and which is strongest at small r) drives a bipolar axial jet.



from the $z = 0$ plane. The accumulation of drain-hole particles constitutes the engine that drives the poloidal electric current that drives the astrophysical jet. The z -symmetry of $\psi(r, z)$ and z -antisymmetry of $I(r, z)$ has been noted previously by Ferreira & Pelletier (1995).

Electromagnetic power flow from this dynamo can also be interpreted in terms of the Poynting flux $\mathbf{S} = \mathbf{E} \times \mathbf{B}/\mu_0$. Azimuthal symmetry applied to Faraday's law shows that E_ϕ is zero for a steady-state situation in which case the z -component of the Poynting flux reduces to $S_z = E_r B_\phi/\mu_0$. Because E_r and B_ϕ are both positive for $z > 0$ whereas E_r is positive while B_ϕ is negative for $z < 0$, it is seen that S_z is positive for $z > 0$ and negative for $z < 0$. Thus, the Poynting flux associated with this dust-driven dynamo injects energy into bipolar astrophysical jets flowing normally outward from the $z = 0$ plane.

One can ask just how close to exactly zero \bar{P}_ϕ has to be in order for a particle to behave as a drain-hole particle. Exact $\bar{P}_\phi = 0$ would enable a particle to spiral down all the way to the center of the central object, an obviously unrealistic situation because the particle would vaporize as it approached the stellar surface. A more realistic question then is how small does \bar{P}_ϕ have to be in order for a drain-hole particle to fall to some specified normalized radius \bar{R}_{small} that is much less than unity. \bar{R}_{small} would presumably be of the order of the radius at which the astrophysical jet starts and so would be of the order of the thickness of the accretion disk or somewhat smaller. Since the dimensionless form of Eq.44 is

$$\bar{H} = \frac{1}{2}(\bar{v}_r^2 + \bar{v}_z^2) + \chi(\bar{r}, \bar{z}) \quad (85)$$

where the effective potential is

$$\chi(\bar{r}, \bar{z}) = \frac{1}{2\bar{r}^2} \left(\bar{P}_\phi - \frac{\langle \omega_{c\sigma} \rangle}{2\Omega_0} \bar{\psi}(\bar{r}, \bar{z}) \right)^2 - \frac{1}{\sqrt{\bar{r}^2 + \bar{z}^2}} \quad (86)$$

and since $\bar{H} \simeq 0$, the turning point for a drain-hole particle is where $\chi(\bar{r}, \bar{z}) \simeq 0$. Because $\bar{\psi}(\bar{r}, \bar{z}) \rightarrow 0$ at small \bar{r} , the inner turning point will therefore be where $\bar{P}_\phi^2 = 2\bar{r}^2/\sqrt{\bar{r}^2 + \bar{z}^2}$. Assuming that the inner turning point is at $\bar{r} \sim \bar{R}_{small}$ and $\bar{z} \simeq 0$, the inner turning point is where $\bar{P}_\phi^2 = 2\bar{R}_{small}$. A sufficient condition for assuming $\bar{P}_\phi \simeq 0$ is thus $\bar{P}_\phi^2 < 2\bar{R}_{small}$, i.e.,

$$-\sqrt{2\bar{R}_{small}} < \bar{L} \cos \theta + \frac{\langle \omega_{c\sigma} \rangle}{2\Omega_0} \bar{\psi}(\bar{r}_*, \bar{z}_*) < \sqrt{2\bar{R}_{small}} \quad (87)$$

and particles satisfying this condition will fall to a normalized radius $\bar{R} < \bar{R}_{small}$. For given \bar{L} , $\langle \omega_{c\sigma} \rangle / 2\Omega_0$, and $\bar{\psi}(\bar{r}_*, \bar{z}_*)$ this corresponds to a narrow range in θ centered about the angle at which \bar{P}_ϕ equals zero exactly. Equation 87 can be expressed as $\cos(\theta + \Delta\theta/2) < \cos \theta < \cos(\theta - \Delta\theta/2)$ where

$$\begin{aligned} \bar{L} \cos(\theta + \Delta\theta/2) &= -\sqrt{2\bar{R}_{small}} - \frac{\langle \omega_{c\sigma} \rangle}{2\Omega_0} \bar{\psi}(\bar{r}_*, \bar{z}_*) \\ \bar{L} \cos(\theta - \Delta\theta/2) &= \sqrt{2\bar{R}_{small}} - \frac{\langle \omega_{c\sigma} \rangle}{2\Omega_0} \bar{\psi}(\bar{r}_*, \bar{z}_*). \end{aligned} \quad (88)$$

Subtracting these two equations from each other shows that the range $\Delta\theta$ for drain-hole particles to reach \bar{R}_{small} is

$$\Delta\theta \simeq \frac{2\sqrt{2\bar{R}_{small}}}{\bar{L} \sin \theta}. \quad (89)$$

The solid angle of incident particles lying between θ and $\theta + \Delta\theta$ is $2\pi \sin \theta \Delta\theta$ and so the fraction f_{dh} of all incident particles with angular momentum \bar{L} that become drain-hole particles and fall to $\bar{R} < \bar{R}_{small}$ is

$$f_{dh} = \frac{2\pi \sin \theta \Delta\theta}{4\pi} = \frac{\sqrt{2\bar{R}_{small}}}{\bar{L}}. \quad (90)$$

6.6. Drain hole dynamo power

The strength of the equilibrium radial electric field produced by drain-hole particles can be estimated as follows: Before any drain-hole particles accumulate at small \bar{r} , there is no radial electric field, but as the drain-hole particles accumulate, the radial outward electric field will develop. The force due to the radial outward electric field will oppose the gravitational and magnetic forces causing the inward motion of the drain-hole particles. The balance between these opposing forces is quantified by the radial equation of motion. In cylindrical un-normalized coordinates the radial equation of motion governing drain-hole particles with $v_z = 0$ in the $z = 0$ plane (where $B_\phi = 0$ due to z -antisymmetry of $I(r, z)$) is

$$m_d \left(\ddot{r} - r\dot{\phi}^2 \right) = q_d \left(E_r + r\dot{\phi}B_z \right) - \frac{m_d MG}{r^2}. \quad (91)$$

B_z is approximately uniform at small r so $\psi \simeq \pi r^2 B_z$ at small r in which case the drain-hole particle condition $P_\phi = m_d r^2 \dot{\phi} + q_d \psi / 2\pi = 0$ implies $\dot{\phi} = -q_d B_z / 2m_d$. On eliminating $\dot{\phi}$ in Eq.91, the radial equation of motion governing drain-hole particles is

$$\begin{aligned} \ddot{r} &= \frac{q_d}{m_d} E_r - r \frac{q_d^2 B_z^2}{4m_d^2} - \frac{MG}{r^2} \\ &\simeq \frac{q_d}{m_d} E_r - \frac{MG}{r^2} \end{aligned} \quad (92)$$

where the second line is for small r . When $E_r = 0$, the drain-hole particles fall inwards with gravitational acceleration, but as E_r builds up because of accumulation at small r of fallen-in positively charged drain-hole particles, Eq.92 shows that this electric field will oppose the gravitational force and retard the infall. The drain-hole particles will continue to fall in and accumulate, thereby increasing E_r until the radially outward repulsive electrostatic force due to E_r becomes so strong as to balance gravity and cause \ddot{r} to vanish. Thus, gravitational force is balanced by the radially outward force from the space charge electric field of the

accumulated positively charged drain-hole particles. The saturation electric field is

$$E_r = \frac{m_d MG}{q_d r^2}. \quad (93)$$

Using $E_r = -\partial V/\partial r$, integration of Eq.93 from large r to the jet radius r_{jet} gives the voltage at the jet to be

$$V_{jet} = \frac{m_d MG}{q_d r_{jet}}. \quad (94)$$

The jet electric current corresponds to the charge per second carried inward by the drain-hole particles. The number of drain-hole particles accreting per second is \dot{M}_{dh}/m_d where \dot{M}_{dh} is the mass accretion rate per second of drain-hole particles and m_d is the mass of an individual drain-hole particle. Thus, the poloidal electric current is

$$I_{jet} = q_d \dot{M}_{dh}/m_d. \quad (95)$$

The jet electric power is

$$P_{jet} = I_{jet} V_{jet} = \frac{\dot{M}_{dh} MG}{r_{jet}} \quad (96)$$

which is just the rate at which gravitational potential energy is released by drain-hole particles falling from large r to the jet radius. The drain-hole dynamo converts the gravitational energy released from accretion into electrical power suitable for driving bipolar jets that are moving away from the $z = 0$ plane. The jet power is proportional to both the central object mass M and the drain-hole mass accretion rate \dot{M}_{dh} . Paper I showed that the dust mass accretion rate can be a substantial fraction of the total mass accretion so P_{jet} can be a substantial fraction of the power of all accreting material. The jet power accelerates the jet material to escape velocity and so is equal to the power available from accreting drain-hole dust grains. Thus, assuming that the axial starting point for jet particles is of the order of r_{jet} , the power required to drive the jet particles to escape velocity is $P_{jet} = \dot{M}_{jet} MG/r_{jet}$ and so the jet mass outflow would be approximately equivalent to the drain hole particle accretion rate, i.e., $\dot{M}_{jet} \simeq \dot{M}_{dh}$. The particles in the jet would not, in general, be the drain hole particles, but instead would be plasma magnetohydrodynamically accelerated using the drain-hole accretion as the power source. Assuming $\bar{L} \simeq 1$ and $\bar{R}_{small} = r_{jet}/a \sim 0.1$ in Eq.90, the fraction of retrograde particles that are drain hole and able to reach r_{jet} would be $f_{dh} = 0.4$; the fraction of combined retrograde and prograde dust grains would thus be 0.2. The example in paper I showed that because of differences in proportional slowing down, the dust accretion rate would be enriched to be 20% of the gas accretion rate. This gives $\dot{M}_{dh}/\dot{M}_g \sim 0.2 \times 0.2 = 0.04$ and so predicts a jet power that would be about 1/25 of the power associated with all accreting dust and gas. This ratio of outflow power to accretion power is

consistent with the estimate given by Bacciotti *et al.* (2004) using HST observations of T Tauri jets.

7. Torque and angular momentum

An important question repeatedly asked about accretion disks and jets is the role played by jets in satisfying conservation of mechanical angular momentum of the accreting material. It will now be shown that mechanical angular momentum is exactly conserved in our model.

Because of axisymmetry, the canonical angular momentum of the j^{th} charged dust grain

$$P_{\phi,d,j}^+ = m_+ r v_\phi^j + Ze\psi(r, z)/2\pi \quad (97)$$

and the canonical angular momentum of the k^{th} electron

$$P_{\phi,k}^e = m_e r v_\phi^k - e\psi(r, z)/2\pi \quad (98)$$

at any position r, z are both invariants, i.e., $P_{\phi,d}^+ = \text{const.}$ and $P_{\phi,k}^e = \text{const.}$ In general, the dust grains and the electrons at any position r, z will have quite different values of v_ϕ but, in order for the plasma to be macroscopically quasi-neutral, there must be approximately Z electrons adjacent to each dust grain. Because electron and dust grain trajectories differ, these neighboring electrons will typically not be the original sibling electrons photo-emitted when the dust grain became charged.

The radial and axial velocities of a specific dust grain or electron can be written as $v_r^{\sigma,j} = dr^{\sigma,j}/dt$ and $v_z^{\sigma,j} = dz^{\sigma,j}/dt$ where $r^{\sigma,j}(t)$ and $z^{\sigma,j}(t)$ are the position of the j^{th} particle of species σ . Since P_ϕ is conserved for each individual particle, the time derivatives of the P_ϕ 's of a dust grain at a location r, z and its neighboring neutralizing Z electrons respectively give $dP_{\phi,d,j}^+/dt = 0$ and $dP_{\phi,k}^e/dt = 0$. Using $d\psi/dt = v_r \partial\psi/\partial r + v_z \partial\psi/\partial z$ for the time derivative of ψ measured in the particle frame, respective time derivatives of Eqs.97 and 98 give

$$\frac{d}{dt} (m_+ r v_\phi^{+,j}) = -\frac{Ze}{2\pi} \left(\frac{\partial\psi}{\partial r} v_r^{+,j} + \frac{\partial\psi}{\partial z} v_z^{+,j} \right) \quad (99)$$

and

$$\frac{d}{dt} (Z m_e r v_\phi^{e,k}) = \frac{Ze}{2\pi} \left(\frac{\partial\psi}{\partial r} v_r^{e,k} + \frac{\partial\psi}{\partial z} v_z^{e,k} \right). \quad (100)$$

Using $B_r = -(2\pi r)^{-1} \partial\psi/\partial z$ and $B_z = (2\pi r)^{-1} \partial\psi/\partial r$ from Eq.7 and summing Eqs.99 and 100 over the dust grains and their associated Z neutralizing electrons at location r, z gives

$$\frac{dL_\phi}{dt} = r (J_z B_r - J_r B_z) = r \hat{\phi} \cdot \mathbf{J}_{pol} \times \mathbf{B}_{pol} \quad (101)$$

where J_r , J_z are the respective radial and axial current densities and L_ϕ is the total mechanical angular momentum density taking into account both dust grains and electrons. Thus, from the macroscopic point of view there is a torque about the z axis, namely $\hat{z} \cdot \mathbf{r} \times \mathbf{F} = \hat{z} \times (r\hat{r} + z\hat{z}) \cdot (\mathbf{J}_{pol} \times \mathbf{B}_{pol}) = r\hat{\phi} \cdot \mathbf{J}_{pol} \times \mathbf{B}_{pol}$ acting to change the local mechanical angular momentum density.

On the other hand, using Eqs.7 and 5 it is seen that when this torque is integrated over the entire volume to infinity,

$$\begin{aligned} \int d^3r r \hat{\phi} \cdot \mathbf{J}_{pol} \times \mathbf{B}_{pol} &= \int d^3r r^2 \nabla \phi \cdot \left(\frac{1}{2\pi} \nabla I \times \nabla \phi \right) \times \left(\frac{1}{2\pi} \nabla \psi \times \nabla \phi \right) \\ &= \frac{1}{4\pi^2} \int d^3r r^2 \nabla \phi \times (\nabla I \times \nabla \phi) \cdot (\nabla \psi \times \nabla \phi) \\ &= \frac{1}{4\pi^2} \int d^3r \nabla I \cdot (\nabla \psi \times \nabla \phi) \\ &= \frac{1}{4\pi^2} \int d^3r \nabla \cdot (I (\nabla \psi \times \nabla \phi)) \\ &= 0 \end{aligned} \quad (102)$$

since both I and $\nabla \psi$ vanish at ∞ . Thus, the total mechanical angular momentum of the system is exactly conserved because there is no net torque applied to the whole system.

I is an odd function of z and ψ is an even function of z , and in the jet \mathbf{J}_{pol} is nearly parallel to \mathbf{B}_{pol} . This suggests the following generic form for the current

$$\mu_0 I(r, z) \simeq \lambda \psi(r, z) \tanh \left(\frac{z}{h(r)} \right) \quad (103)$$

where $h(r)$ represents the height of the accretion disk at radius r and λ , the current per flux, has units of inverse length. Thus far from the $z = 0$ plane, Eq.103 has the form $\mu_0 I/\psi = \lambda \text{sign}(z)$ so that the jet above the $z = 0$ plane has the opposite handedness of the jet below the $z = 0$ plane. The parameter λ is closely related to the current per flux in a force-free system (i.e., a system satisfying $\nabla \times \mathbf{B} = \lambda \mathbf{B}$), but differs slightly because here λ refers to just the ratio of the poloidal current to the poloidal flux. Using Eq.101 it is seen that the density of MHD torque about the z axis is of the generic form

$$\begin{aligned} \frac{dL_\phi}{dt} &= \frac{1}{4\pi^2 r} \left(-\frac{\partial I}{\partial r} \frac{\partial \psi}{\partial z} + \frac{\partial I}{\partial z} \frac{\partial \psi}{\partial r} \right) \\ &= \frac{\lambda}{4\mu_0 \pi^2 r} \left\{ -\frac{\partial}{\partial r} \left[\psi(r, z) \tanh \left(\frac{z}{h(r)} \right) \right] \frac{\partial \psi}{\partial z} + \frac{\partial}{\partial z} \left[\psi(r, z) \tanh \left(\frac{z}{h(r)} \right) \right] \frac{\partial \psi}{\partial r} \right\}. \end{aligned} \quad (104)$$

We assume that $\partial h / \partial r \ll 1$ so the radial scale length at which h changes is much larger than h . Also, from symmetry $\partial \psi / \partial z = 0$ on the $z = 0$ midplane. Together, these conditions imply that near the midplane the last term in Eq.104 dominates so near the midplane

$$\frac{dL_\phi}{dt} \simeq \frac{\lambda}{4\mu_0 \pi^2 h r} \frac{\psi(r, z)}{\cosh^2(z/h)} \frac{\partial \psi}{\partial r} = \frac{\lambda \psi(r, z)}{2\pi \mu_0 h} \frac{B_z(r, z)}{\cosh^2(z/h)}. \quad (105)$$

As seen from Eq.102 the torque density is proportional to $-\nabla I \times \nabla \phi \cdot \nabla \psi \sim -r \mathbf{J}_{pol} \cdot \nabla \psi$ and so is positive for poloidal current flow away from the poloidal field magnetic axis and negative for poloidal current flow towards the poloidal field magnetic axis. The torque density vanishes as $r \rightarrow 0$ and as $r \rightarrow \infty$ and at the poloidal field magnetic axis because $r \nabla \psi \rightarrow 0$ at $r = 0$, $\mathbf{J}_{pol} \rightarrow 0$ at $r = \infty$, and $\nabla \psi = 0$ at the poloidal field magnetic axis. The direction of poloidal current flow is shown in Fig.13. This torque acts on the drain hole particles and their associated electrons since these particles are the carriers of the poloidal current as sketched in Fig.12 and Fig.13. Unlike the drain-hole particles, no torque $r \hat{\phi} \cdot \mathbf{J} \times \mathbf{B}$ about the z axis acts on the Speiser particles because the current associated with the Speiser particles is in the ϕ direction.

8. Conclusions

We have shown that charging of collisionless dust grains incident upon a star causes the dust grain orbital dynamics to change from a relatively simple Kepler form to more complicated motion involving competition between magnetic and gravitational forces. This competition gives rise to five qualitatively different types of orbits. Two of these, the retrograde and prograde cometary orbits are just perturbations of Kepler cometary orbits. The orbit of a particle where magnetic forces overwhelm gravitational forces is just a Larmor (cyclotron) orbit and in this case the particle is constrained to remain within a poloidal Larmor radius of a poloidal flux surface in a manner similar to tokamak confinement. Particles where magnetic and gravitational forces are comparable can have two very different types of orbit depending on whether the incident particle is prograde or retrograde. Prograde particles of this latter type develop Speiser orbits; these orbits are paramagnetic with respect to the poloidal magnetic field and so can be the source of the poloidal magnetic field. Retrograde particles having comparable magnetic and gravitational forces can have a peculiar behavior whereby centrifugal force is eliminated with the result that the charged particle falls in towards the star along a spiral orbit. The accumulation of these “drain-hole” particles near the star provides a radial electric field oriented so as to drive the poloidal currents and toroidal magnetic fields of an astrophysical jet.

This paper showed the existence of these different types of orbits, how their orientation is suitable for generating the poloidal and toroidal magnetic fields associated with an accretion disk and astrophysical jet, and how questions of angular momentum conservation are inherently resolved. A future paper will investigate the quantitative values of dust grain parameters required to produce toroidal and poloidal fields in the accretion disk of a young stellar object.

Finally, we offer some remarks regarding the effect of deviations from axisymmetry. The model presented here assumed perfect magnetic field axisymmetry whereas actual accretion disks are observed to have varying amounts of non-axisymmetry. This situation is analogous to toroidal magnetic fusion devices such as tokamaks, reversed field pinches, and spheromaks all of which are modeled to first approximation as being axisymmetric, but in reality have deviations from axisymmetry due to waves, turbulence, instability, and errors in machine construction. It is known from these devices that a modest breaking of symmetry does not invalidate the results of the axisymmetric model, but rather weakens the conclusions, e.g., instead of cyclotron-orbiting particles being perfectly confined to the vicinity of a poloidal flux surface, when there is deviation from axisymmetry cyclotron-orbiting particles can slowly wander away from the poloidal flux surface they started on. One would expect that deviations from axisymmetry in accretion disks would cause a similar transport of cyclotron particles across poloidal flux surfaces. Because symmetry breaking causes the canonical angular momentum of particles to change, it could be considered as being somewhat like a collision that changes the canonical angular momentum of each of two particles involved in a collision while conserving the total canonical angular momenta. Hence, deviations from axisymmetry would cause a jiggling of the canonical angular momenta of individual particles so that particles on the borderline between being drain-hole and cyclotron or on the borderline between being Speiser and cyclotron might spend part of the time (i.e., between jiggles) being one type and part of the time being the neighboring type. Similarly cyclotron particles that are on the borderline between being mirror-trapped and not mirror-trapped would, as they get kicked into and out of the mirror loss-cone, spend part of the time being mirror-trapped and part of the time not being mirror-trapped. However, at any given time there would be a certain fraction of particles of each type, i.e., a certain fraction would be cyclotron, a certain fraction would be drain-hole, a certain fraction would be Speiser, and a certain fraction would be cometary.

APPENDICES

A. Derivation of generic poloidal flux function

If all the toroidal current \mathcal{I}_ϕ is concentrated at the poloidal location $r = R_0$ and $z = 0$, then the toroidal current density is $\mathbf{J}_{tor} = \hat{\phi} \mathcal{I}_\phi \delta(z) \delta(r - R_0)$. On defining

$$k^2 = \frac{4R_0 r}{(R_0 + r)^2 + z^2} \quad (\text{A1})$$

analytic solution of Eq.6 using $\mathbf{J}_{tor} = \hat{\phi} \mathcal{I}_\phi \delta(z) \delta(r - R_0)$ gives (Jackson 1999)

$$\psi(r, z) = \frac{\mu_0 \mathcal{I}_\phi}{k} \sqrt{R_0 r} [(2 - k^2) K(k) - 2E(k)] \quad (\text{A2})$$

where E and K are complete elliptic integrals. Equation A2 describes the situation where all the current density is concentrated at $r = R_0$, $z = 0$, i.e., the current flows in a wire of zero cross-section located at $r = R_0$, $z = 0$. This equation can also be used to (i) describe the field observed at locations far from the poloidal field magnetic axis of a distributed current localized in the vicinity of the poloidal field magnetic axis and (ii) as the Green's function for a distributed toroidal current. This is because for an observer who is far from $r = R_0$, $z = 0$, the field of a distributed toroidal current localized near $r = R_0$, $z = 0$ is indistinguishable from the field of a zero cross-section wire carrying the same total current. Equation A2 has a logarithmic singularity at the wire location because the wire has infinitesimal diameter.

Two analytic limits are of interest for Eq.A2. The first is where $r \ll R_0$ so

$$k^2 \simeq \frac{4R_0 r}{R_0^2 + z^2} \quad (\text{A3})$$

and the second is where $r \gg R_0$ so

$$k^2 \simeq \frac{4R_0 r}{r^2 + z^2}. \quad (\text{A4})$$

The former gives the field near the loop axis and the latter gives the field at locations far from the current loop. In both cases k^2 is small compared to unity and so the small argument asymptotic expansions of the complete elliptic integrals can be used, namely,

$$E(k) = \frac{\pi}{2} \left(1 - \frac{k^2}{4} - \frac{3}{64} k^4 - \dots \right), \quad K(k) = \frac{\pi}{2} \left(1 + \frac{k^2}{4} + \frac{9}{64} k^4 + \dots \right). \quad (\text{A5})$$

Thus for small k , it is seen that $(2 - k^2) K(k) - 2E(k) \simeq \pi k^4/16$ in which case

$$\psi(r, z) = \frac{\pi\mu_0\mathcal{I}_\phi}{2} \frac{R_0^2 r^2}{((R_0 + r)^2 + z^2)^{3/2}} \quad (\text{A6})$$

so for $r \ll R_0$

$$\lim_{r \ll a} \psi(r, z) \simeq \frac{\pi\mu_0\mathcal{I}_\phi}{2} \frac{R_0^2 r^2}{(R_0^2 + z^2)^{3/2}} \quad (\text{A7})$$

and for $r \gg R_0$

$$\lim_{r \gg a} \psi(r, z) \simeq \frac{\pi\mu_0\mathcal{I}_\phi}{2} \frac{R_0^2 r^2}{(r^2 + z^2)^{3/2}}. \quad (\text{A8})$$

For purposes of discussion and also numerical computation, it is convenient to choose Eq.A6 to represent the poloidal flux of a generic toroidal current *everywhere*. Making this choice for the poloidal flux function (instead of the prescription given by Eq.A2) means that $\psi(r, z)$ has a smooth hill-top at $r = 2R_0$ rather than a logarithmic singularity at $r = R_0$ and has the same behavior far from $r = R_0, z = 0$ as does Eq.A2.

Thus, a useful analytic representation for a nonsingular, physically realizable flux function is obtained by recasting Eq.A6 in the form

$$\psi(r, z) = \frac{27 (r/a)^2}{8 \left(\left(\frac{r}{a} + \frac{1}{2} \right)^2 + \left(\frac{z}{a} \right)^2 \right)^{3/2}} \psi_0. \quad (\text{A9})$$

This has a maximum of ψ_0 at $r = a$, scales as r^2 for small r , and scales as r^{-1} for large r . Equation 6 can be used to calculate the associated toroidal current density which will be sharply peaked near $r = a$ and $z = 0$. The $\psi(r, z)$ prescribed by Eq.A9 has the features that it provides a dipole-like field far from the z axis and a nearly uniform axial field near the z axis, corresponds to a realistic distributed toroidal current, has a well-defined poloidal field magnetic axis, is analytically tractable, and is convenient for numerical computation of representative particle orbits in a physically relevant magneto-gravitational field.

B. Current associated with flux function

Using Ampere's law to relate the toroidal current and the poloidal magnetic field it is seen that

$$\mathcal{I}_\phi = \frac{1}{\mu_0} \oint_C \mathbf{B}_{pol} \cdot d\mathbf{l} \quad (\text{B1})$$

where the contour C links the total toroidal current \mathcal{I}_ϕ . By letting the line integral go to infinity in the radial and z directions it is seen that only the portion of the line integral along

the z axis makes a finite contribution so

$$\begin{aligned}\mathcal{I}_\phi &= \frac{1}{\mu_0} \int_{-\infty}^{\infty} B_z(0, z) dz \\ &= \frac{27\psi_0}{16\pi\mu_0} \lim_{r \rightarrow 0} \frac{1}{r} \frac{\partial}{\partial r} \left(\frac{r^2}{a^2} \int_{-\infty}^{\infty} \frac{dz}{\left(\left(\frac{r}{a} + \frac{1}{2}\right)^2 + \left(\frac{z}{a}\right)^2\right)^{3/2}} \right) .\end{aligned}\tag{B2}$$

Defining $b = r/a + 1/2$ and $z/a = b \sinh \vartheta$ the z integral can be expressed as

$$\begin{aligned}\int_{-\infty}^{\infty} \frac{dz}{\left(\left(\frac{r}{a} + \frac{1}{2}\right)^2 + \left(\frac{z}{a}\right)^2\right)^{3/2}} &= a \int_{-\infty}^{\infty} \frac{b \cosh \vartheta d\vartheta}{(b^2 + b^2 \sinh^2 \vartheta)^{3/2}} \\ &= \frac{a}{b^2} [\tanh \vartheta]_{-\infty}^{\infty} \\ &= \frac{2a}{(r/a + 1/2)^2} .\end{aligned}\tag{B3}$$

Since

$$\lim_{r \rightarrow 0} \frac{1}{r} \frac{\partial}{\partial r} \left[\frac{r^2}{a^2} \frac{2a}{(r/a + 1/2)^2} \right] = \frac{16}{a}\tag{B4}$$

the total toroidal current is

$$\mathcal{I}_\phi = \frac{27\psi_0}{\pi a \mu_0} .\tag{B5}$$

C. Review: Distinction between diamagnetic (adiabatic) orbits and paramagnetic (Speiser) orbits

C.1. Diamagnetism of cyclotron (Larmor) orbits

We first review charged particle motion in a uniform magnetic field $\mathbf{B} = B_z \hat{z}$ (so $\psi = B_z \pi r^2$) and no electric field; orbital motion in more complex fields will be discussed later. The particle motion is prescribed by the Lorentz equation

$$m_\sigma \frac{d\mathbf{v}}{dt} = q_\sigma \mathbf{v} \times B_z \hat{z} .\tag{C1}$$

If the particle is restricted to the $z = 0$ plane, the respective radial and azimuthal components of Eq.C1 are

$$m_\sigma \left(\ddot{r} - r \dot{\phi}^2 \right) = q_\sigma r \dot{\phi} B_z\tag{C2}$$

$$\frac{m_\sigma}{r} \frac{d}{dt} \left(r^2 \dot{\phi} \right) = -q_\sigma \dot{r} B_z .\tag{C3}$$

We consider circular motion (i.e., cyclotron or Larmor orbits) so $r = \text{const.}$ in which case Eq.C3 gives $\dot{\phi} = \text{const.}$ and Eq.C2 then becomes

$$\dot{\phi} = -\omega_{c\sigma}\tag{C4}$$

where $\omega_{c\sigma} = q_\sigma B_z / m_\sigma$ is the signed cyclotron frequency. The minus sign in Eq.C4 indicates that cyclotron motion is *diamagnetic*. Thus if a gyrating charged particle is considered as a ϕ -directed current, the polarity of this current is such as to create a magnetic field which opposes the initial field B_z , i.e., cyclotron orbits tend to depress the value of ψ . The diamagnetism of cyclotron orbits means that cyclotron orbits cannot be the source for the assumed poloidal magnetic field $\psi(r, z)$ nor the means by which this field is sustained against dissipation.

C.2. Adiabatic orbits

When the magnetic field is non-uniform or there are electric fields, and if these additional features are sufficiently weak that to lowest order the Larmor orbit (cyclotron orbit) description is approximately correct, then additional charged particle motions occur which are superimposed on the Larmor orbits $\mathbf{v}_L(t)$; these additional motions are adiabatic in the sense of classical mechanics. Defining v_\parallel as the velocity component parallel to the magnetic field and \mathbf{v}_\perp as the component perpendicular to the magnetic field these motions are the standard drifts (Longmire 1967; Chen 1984), namely the $E \times B$ drift $\mathbf{v}_E = \mathbf{E} \times \mathbf{B} / B^2$, the polarization drift $\mathbf{v}_p = m_\sigma q_\sigma^{-1} B^{-2} d\mathbf{E}_\perp / dt$, the curvature drift $\mathbf{v}_c = -m_\sigma v_\parallel^2 \hat{B} \cdot \nabla \hat{B} \times \mathbf{B} / q_\sigma B^2$, and the grad B drift $\mathbf{v}_{\nabla B} = -\mu \nabla B \times \mathbf{B} / q_\sigma B^2$ where $\mu = m_\sigma v_\perp^2 / 2B$ is the magnetic moment, an adiabatic invariant. There is also a ‘force’ drift $\mathbf{v}_F = \mathbf{F} \times \mathbf{B} / q_\sigma B^2$ where \mathbf{F} is a generic non-electromagnetic force, which here is gravity, so $\mathbf{F} = mMG\nabla(r^2 + z^2)^{-1/2}$. Taking into account all these drifts, the velocity of an adiabatic-orbit charged particle becomes

$$\begin{aligned} \mathbf{v} = & v_\parallel \hat{B} + \mathbf{v}_{L\sigma}(t) + \frac{\mathbf{E} \times \mathbf{B}}{B^2} + \frac{m_\sigma}{q_\sigma B^2} \frac{d\mathbf{E}_\perp}{dt} - \frac{m_\sigma v_\parallel^2 \hat{B} \cdot \nabla \hat{B} \times \mathbf{B}}{q_\sigma B^2} \\ & - \frac{\mu \nabla B \times \mathbf{B}}{q_\sigma B^2} + \frac{m_\sigma MG}{q_\sigma B^2} \nabla \left(\frac{1}{\sqrt{r^2 + z^2}} \right) \times \mathbf{B}. \end{aligned} \quad (\text{C5})$$

The last four drifts in Eq.C5 explicitly involve q_σ and thus produce macroscopic currents. When these currents are summed and, in addition, diamagnetic current is taken into account, the result is equivalent to the MHD equation of motion where the polarization drift plays the role of the inertial term (Goldston & Rutherford 1995; Bellan 2006). The ideal MHD concept of frozen-in flux is directly equivalent to μ conservation because μ conservation corresponds to conservation of the magnetic flux linked by a cyclotron orbit. Thus, the ideal MHD concept of frozen-in flux is based on the adiabatic invariance of cyclotron orbits.

The poloidal flux function specified by Eq.9 corresponds to a magnetic field generated by a toroidal current flowing in the positive ϕ direction (counterclockwise direction); the B_z component of this field is positive for $r < a$ and negative for $r > a$ where a is the location of the poloidal field magnetic axis. The poloidal magnetic field has both curvature and gradients

so that away from field nulls, particles should have parallel motion and cyclotron orbits together with superimposed curvature and grad B drifts. Figure 14 shows the numerically calculated orbit of a particle located in the $z = 0$ plane in a magnetic field prescribed by Eq.9 and located inside the poloidal field magnetic axis (indicated by dashed circle). It is seen that the particle makes cyclotron orbits with a superimposed drift due to curvature and ∇B . The cyclotron orbit is clockwise consistent with the assertion that cyclotron motion is diamagnetic. Figure 15 shows the situation for a particle located at a radius outside the poloidal field magnetic axis. The sense of the cyclotron orbit is now reversed as is the polarity of B_z so the cyclotron orbit is again diamagnetic. For both inside and outside particles the drift motion is clockwise and so opposes the original toroidal current creating the poloidal flux and so the curvature and ∇B drift motion can also be considered diamagnetic.

The current associated with the gravitational force drift is

$$\mathbf{J}_g = \sum_{\sigma} n_{\sigma} q_{\sigma} \mathbf{v}_F = \frac{\varrho MG}{B^2} \nabla \left(\frac{1}{\sqrt{r^2 + z^2}} \right) \times \mathbf{B} \quad (\text{C6})$$

where $\varrho = \sum m_{\sigma} n_{\sigma}$ is the mass density.

From a macroscopic (i.e., MHD) point of view, the force associated with the gravitational drift current exactly balances the gravitational force component perpendicular to the magnetic field since

$$\begin{aligned} \mathbf{J}_g \times \mathbf{B} &= \frac{\varrho MG}{B^2} \left(\nabla \left(\frac{1}{\sqrt{r^2 + z^2}} \right) \times \mathbf{B} \right) \times \mathbf{B} \\ &= -\varrho MG \nabla_{\perp} \left(\frac{1}{\sqrt{r^2 + z^2}} \right) \end{aligned} \quad (\text{C7})$$

If $I = 0$ on the $z = 0$ plane (as is consistent with astrophysical jet symmetry used by Lovelace (1976)), the gravitational drift is not defined on the poloidal field magnetic axis because \mathbf{B} vanishes on the poloidal field magnetic axis and the theory of particle drifts fails. In other words, going from the first to the second line in Eq.C7 at the poloidal field magnetic axis would involve dividing zero by zero (since $B = 0$ on the poloidal field magnetic axis).

When summed over species, the curvature and grad B drifts correspond to currents which balance macroscopic pressure gradients (when diamagnetic current is included) and the polarization current corresponds to the inertial term in the MHD equation of motion. This analysis shows, as discussed in Bellan (2007), that plasma particles undergoing cyclotron motion and drifts do not have Keplerian orbits. It also shows that the poloidal field magnetic axis is a special place where conventional particle drift theory fails.

Fig. 14.— Orbit of a positive particle in the $z = 0$ plane located inside the poloidal field magnetic axis (indicated by dashed circle), coordinates are normalized to the poloidal field magnetic axis radius. B_z is positive inside the circle and negative outside.

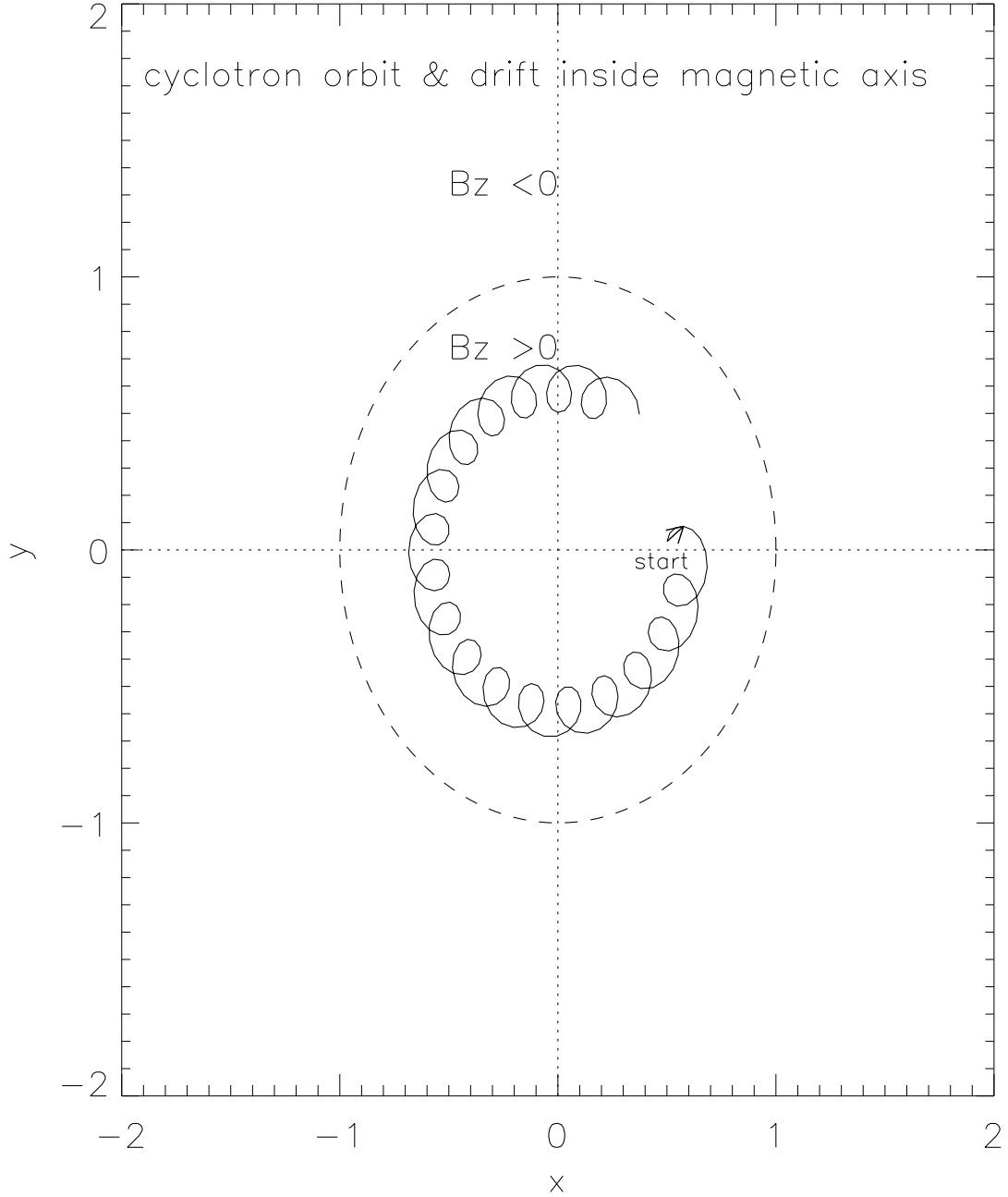
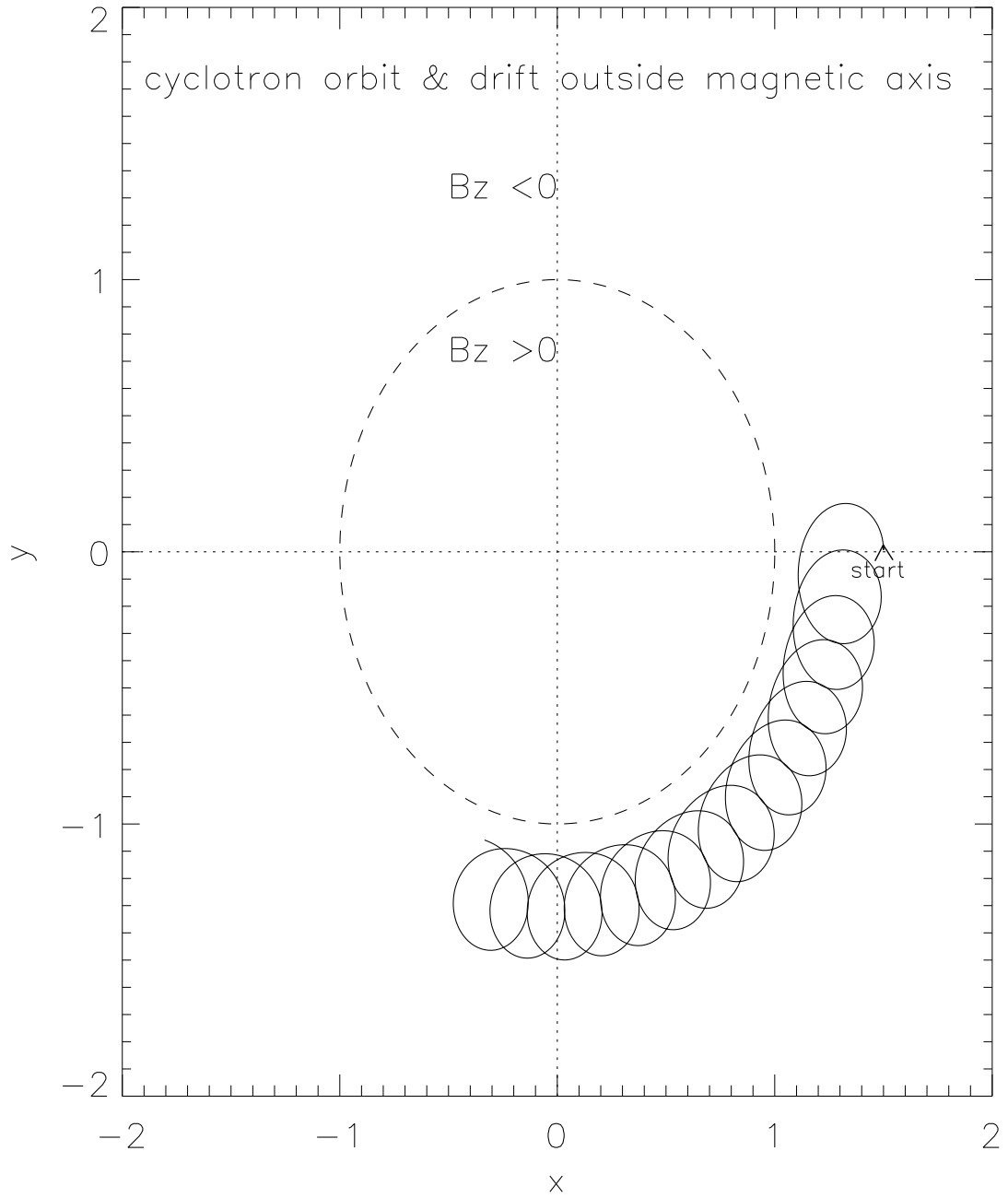


Fig. 15.— Orbit for a positively charged particle located in the z plane outside the poloidal field magnetic axis (dashed circle).



C.3. Non-adiabatic motion: the Speiser orbit

An extreme form of magnetic non-uniformity occurs where the magnetic field reverses direction. In this case an orbit quite distinct from the cyclotron orbit and its associated adiabatic drifts occurs. This non-adiabatic orbit, called a meandering or Speiser orbit (Speiser 1965), consists of semi-circles of counterclockwise motion interspersed with semi-circles of clockwise motion.

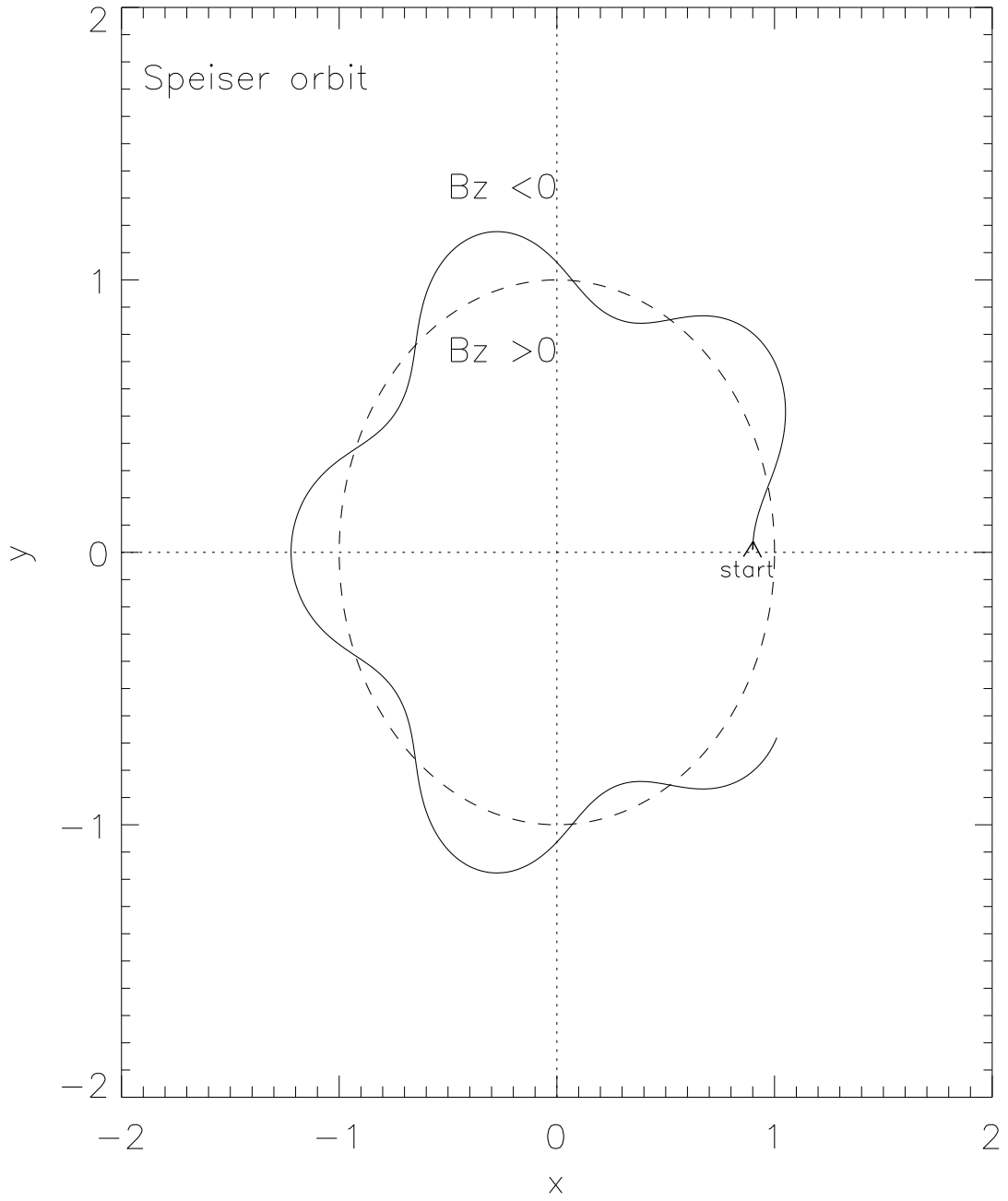
A numerically calculated Speiser orbit for a positively charged particle in the $z = 0$ plane is shown in Fig.16. The particle oscillates across the poloidal field magnetic axis between the inside region where $B_z > 0$ and the outside region where $B_z < 0$. The result is a net counterclockwise motion so, in contrast to cyclotron orbits, Speiser orbits are *paramagnetic*. The paramagnetism of Speiser orbits has been considered an important aspect of current sheets in Earth’s magnetotail, [e.g., see Zelenyi *et al.* (2000)], but to the author’s knowledge this paramagnetism has not been previously considered in the axisymmetric three-dimensional geometry discussed here which is relevant to accretion disks and astrophysical jets. In particular, we will show that the poloidal flux function can be considered as a consequence of Speiser orbits such as shown in Fig.16. Speiser orbits are not consistent with the drift approximation (i.e., $E \times B$ drift, grad B drift, curvature drift, etc.) because the drift approximation is based on the assumption that, to lowest order, the particle is undergoing cyclotron motion. The inconsistency between Speiser orbits and the drift approximation is obvious when one considers that the drift approximation fails where B reverses polarity whereas Speiser orbits depend on this reversal.

If motion in the z direction is also allowed, then because B_r also reverses at the poloidal field magnetic axis, the particle can also oscillate vertically across the poloidal field magnetic axis to make vertical Speiser orbits. The combined r and z Speiser motion means that particles moving at an arbitrary angle across the poloidal field magnetic axis will reflect from interior surfaces of the nested poloidal flux surfaces concentric with the poloidal field magnetic axis. These nested poloidal flux surfaces can thus be imagined as the walls of a toroidal tunnel and the Speiser orbit particles can be considered as reflecting from the interior walls of this toroidal tunnel while moving in the counterclockwise direction to trace out paramagnetic orbits and create poloidal flux.

D. Equation of motion and its solutions

The Hamiltonian orbit analysis presented here shows that photo-emission creates new effective potential barriers. The topography of these barriers depends on a combination of

Fig. 16.— Speiser orbit. The charged particle bounces back and forth across the field null at the poloidal field magnetic axis resulting in a counterclockwise (i.e., paramagnetic) orbit.



environmental factors, particle properties, and the location of the charging. Representative orbits obtained by numerically integrating the equation of motion have been presented and are consistent with the predictions of the Hamiltonian theory. We outline here the derivation of the dimensionless equation of motion; this derivation gives insights into several fundamental issues regarding the dynamics, especially the influence of initial conditions.

The equation of motion for a charged particle in a combined electromagnetic and gravitational field is

$$m_\sigma \frac{d^2 \mathbf{x}}{dt^2} = q_\sigma (\mathbf{E} + \mathbf{v} \times \mathbf{B}) + m_\sigma MG \nabla \frac{1}{\sqrt{r^2 + z^2}}. \quad (\text{D1})$$

Using Eq.1 for the magnetic field, the equation of motion can thus be written as

$$\begin{aligned} m_\sigma \frac{d^2 \mathbf{x}}{dt^2} = & q_\sigma \mathbf{E} \\ & + \frac{q_\sigma}{2\pi} \frac{d\mathbf{x}}{dt} \times \left(\frac{\partial \psi}{\partial \mathbf{x}} \times \frac{\partial \phi}{\partial \mathbf{x}} + \mu_0 I \frac{\partial \phi}{\partial \mathbf{x}} \right) \\ & + m_\sigma MG \nabla \left(\frac{1}{\sqrt{r^2 + z^2}} \right). \end{aligned} \quad (\text{D2})$$

Then, using the definitions given in Eq.57, the equation of motion can be expressed in dimensionless form as

$$\frac{d^2 \bar{\mathbf{x}}}{d\tau^2} = \bar{\mathbf{E}} + \frac{\langle \omega_{c\sigma} \rangle}{2\Omega_0} \frac{d\bar{\mathbf{x}}}{d\tau} \times \left(\frac{\partial \bar{\psi}}{\partial \bar{\mathbf{x}}} \times \frac{\partial \phi}{\partial \bar{\mathbf{x}}} + \frac{\mu_0 I}{a\pi \langle B_z \rangle} \frac{\partial \phi}{\partial \bar{\mathbf{x}}} \right) - \frac{\bar{\mathbf{x}}}{|\bar{\mathbf{x}}|^3} \quad (\text{D3})$$

where

$$\bar{\mathbf{E}} = \frac{q_\sigma}{am_\sigma \Omega_0^2} \mathbf{E} = -\frac{q_\sigma}{a^2 m_\sigma \Omega_0^2} \frac{\partial V}{\partial \bar{\mathbf{x}}} = -\frac{\partial \bar{V}}{\partial \bar{\mathbf{x}}} \quad (\text{D4})$$

is the dimensionless electric field and

$$\bar{V} = \frac{aq_\sigma V}{m_\sigma MG} \quad (\text{D5})$$

is the dimensionless electrostatic potential.

Equation D3 clearly shows that the dynamics change from being gravitationally dominated to being magnetically dominated according to the ratio $\langle \omega_{c\sigma} \rangle / \Omega_0$. The possibility of complex interactions between gravitational and magnetic forces when $\langle \omega_{c\sigma} \rangle / \Omega_0$ is of order unity is also evident. The coefficient $\mu_0 I / a\pi \langle B_z \rangle$ is related to the pitch of a twisted field. The Hamilton-Lagrange formalism shows that I plays a subservient role for particle orbits compared to ψ because canonical angular momentum depends on ψ , not I . However, large I increases $|B|$ and so contributes to the effective potential $\mu|B|$ thereby providing additional possibilities for localization. Thus, if μ is large, a particle is not only constrained to stay on a constant ψ surface, but is additionally constrained to stay out of regions on this surface where $\mu|B|$ is large. If poloidal currents flow, then the associated $\mathbf{J}_{pol} \times \mathbf{B}_{tor}$ forces drive jets

which inflate and distend the ψ surfaces. Thus, the orbits will depend indirectly on I when the jet dynamics alter the shape of the constant ψ surfaces.

Using the relations

$$\begin{aligned}\frac{\partial\phi}{\partial\mathbf{x}} &= \frac{\hat{\phi}}{\bar{r}} = \frac{-\hat{x}\bar{y}+\hat{y}\bar{x}}{\bar{x}^2+\bar{y}^2} \\ \frac{\partial\bar{\psi}}{\partial\mathbf{x}} &= \frac{\partial\bar{\psi}}{\partial\bar{r}}\hat{r} + \frac{\partial\bar{\psi}}{\partial\bar{z}}\hat{z} = \frac{\partial\bar{\psi}}{\partial\bar{r}}\left(\frac{\hat{x}\bar{x}+\hat{y}\bar{y}}{\sqrt{\bar{x}^2+\bar{y}^2}}\right) + \frac{\partial\bar{\psi}}{\partial\bar{z}}\hat{z},\end{aligned}\tag{D6}$$

the normalized equation of motion can be expressed in Cartesian coordinates as

$$\begin{aligned}\frac{d^2\bar{\mathbf{x}}}{d\tau^2} &= -\frac{\partial\bar{V}}{\partial\bar{\mathbf{x}}} \\ &+ \frac{\langle\omega_{c\sigma}\rangle}{2\bar{r}\Omega_0}\frac{d\bar{\mathbf{x}}}{d\tau} \times \left(\frac{\frac{\partial\bar{\psi}}{\partial\bar{r}}\hat{z} - \frac{\partial\bar{\psi}}{\partial\bar{z}}\frac{\bar{\mathbf{r}}}{\bar{r}}}{+ \frac{\mu_0 I}{a\pi\langle B_z\rangle}\frac{(-\hat{x}\bar{y}+\hat{y}\bar{x})}{\bar{r}}} \right) \\ &- \frac{(\bar{\mathbf{r}}+\bar{z}\hat{z})}{|\bar{r}^2+\bar{z}^2|^{3/2}}\end{aligned}\tag{D7}$$

where $\bar{\mathbf{r}} = \bar{x}\hat{x} + \bar{y}\hat{y}$ and $\bar{r} = \sqrt{\bar{x}^2 + \bar{y}^2}$. Equation D7 is in a form suitable for numerical computation and has been used to provide the orbital plots shown earlier.

At this point it is convenient to use the generic poloidal flux function given by Eq.9 so the unity-maximum, dipole-like, normalized flux function will be

$$\bar{\psi}(\bar{r}, \bar{z}) = \frac{27\bar{r}^2}{8\left(\left(\bar{r} + \frac{1}{2}\right)^2 + \bar{z}^2\right)^{3/2}}\tag{D8}$$

with

$$\frac{\partial\bar{\psi}}{\partial\bar{r}} = \frac{27\bar{r}\left(\bar{r} + 1 + 4\bar{z}^2 - 2\bar{r}^2\right)}{16\left(\left(\bar{r} + \frac{1}{2}\right)^2 + \bar{z}^2\right)^{5/2}}\tag{D9}$$

and

$$\frac{\partial\bar{\psi}}{\partial\bar{z}} = -\frac{81\bar{r}^2\bar{z}}{8\left(\left(\bar{r} + \frac{1}{2}\right)^2 + \bar{z}^2\right)^{5/2}}.\tag{D10}$$

Thus, the normalized poloidal magnetic field components are

$$\bar{B}_r = \frac{81\bar{r}\bar{z}}{16\pi\left(\left(\bar{r} + \frac{1}{2}\right)^2 + \bar{z}^2\right)^{5/2}}\tag{D11}$$

and

$$\bar{B}_z = \frac{27\left(\bar{r} + 1 + 4\bar{z}^2 - 2\bar{r}^2\right)}{32\pi\left(\left(\bar{r} + \frac{1}{2}\right)^2 + \bar{z}^2\right)^{5/2}}.\tag{D12}$$

We now consider the problem of establishing appropriate initial conditions for an incoming neutral particle. For purposes of starting a computation we assume the particle is located at some initial radial position $\bar{\rho}_0$ in the orbital plane such that $\bar{\rho}_0 > \bar{\rho}_{pericenter}$ where $\bar{\rho}_{pericenter}$ is given by Eq.27. Solving Eq.25 for the initial inward radial velocity gives

$$\bar{v}_{\rho 0} = -\sqrt{2\bar{H} - \frac{\bar{L}^2}{\bar{\rho}_0^2} + \frac{2}{\bar{\rho}_0}}. \quad (D13)$$

and the corresponding initial orbital frame azimuthal velocity is

$$\bar{v}_{\eta 0} = \frac{\bar{L}}{\bar{\rho}_0}. \quad (D14)$$

Equation 30 can be solved for the initial polar angle in the orbital frame as

$$\eta = \alpha + \cos^{-1} \left(\frac{1 - \bar{L}^2/\bar{\rho}_0}{\sqrt{1 + 2\bar{L}^2/\bar{H}}} \right). \quad (D15)$$

Using Eq.31 the initial orbital frame Cartesian coordinates are thus

$$\begin{aligned} \bar{x}' &= \frac{\bar{L}^2 \cos \eta_0}{1 - \sqrt{1 + 2\bar{L}^2/\bar{H}} \cos(\eta_0 - \alpha)} \\ \bar{y}' &= \frac{\bar{L}^2 \sin \eta_0}{1 - \sqrt{1 + 2\bar{L}^2/\bar{H}} \cos(\eta_0 - \alpha)} \\ \bar{z}' &= 0. \end{aligned} \quad (D16)$$

The orbital frame Cartesian velocity components are related to the orbital frame cylindrical velocity components by

$$\begin{aligned} \bar{v}_{x'0} &= \bar{v}_{\rho 0} \cos \eta_0 - \bar{v}_{\eta 0} \sin \eta_0 \\ \bar{v}_{y'0} &= \bar{v}_{\rho 0} \sin \eta_0 + \bar{v}_{\eta 0} \cos \eta_0 \\ \bar{v}_{z'0} &= 0. \end{aligned} \quad (D17)$$

We now take into account that the orbital frame Cartesian coordinate system is rotated by the angle of inclination θ about the x axis with respect to the lab frame coordinate system. The x and x' components of both position and velocity are the same in the two frames but the y and z components are related by

$$\begin{aligned} \bar{y} &= -\bar{z}' \sin \theta + \bar{y}' \cos \theta \\ \bar{z} &= \bar{z}' \cos \theta + \bar{y}' \sin \theta. \end{aligned} \quad (D18)$$

Since \bar{z}' is by definition zero in the orbital frame, the initial lab frame Cartesian coordinates are

$$\begin{aligned} \bar{x}_0 &= \bar{x}'_0 \\ \bar{y}_0 &= \bar{y}'_0 \cos \theta \\ \bar{z}_0 &= \bar{y}'_0 \sin \theta. \end{aligned} \quad (D19)$$

Since v'_z is similarly zero in the orbital frame, in analogy to Eq.D19, the initial lab frame Cartesian velocities are

$$\begin{aligned}\bar{v}_{x0} &= \bar{v}_{x'0} \\ \bar{v}_{y0} &= \bar{v}_{y'0} \cos \theta \\ \bar{v}_{z0} &= \bar{v}_{y'0} \sin \theta.\end{aligned}\tag{D20}$$

Thus, if one wishes to start the numerical computation at the radius $\bar{\rho}_0$ on the trajectory of an incoming particle with orbit parameters $\{\bar{H}, \bar{L}, \theta, \alpha\}$, Eqs.D13, D14, D15, D19 and D20 give the appropriate initial position and velocity lab frame Cartesian components. Before charging, the orbits are degenerate with respect to choice of θ or α , but after charging there is a strong dependence on these two angles. In particular, if $0 \leq \theta < 90^\circ$ the orbit is prograde and Speiser type orbits are possible if the charging occurs near the poloidal field magnetic axis. On the other hand if $90^\circ < \theta \leq 180^\circ$ the orbit is retrograde and drain-hole orbits are possible. Thus, a subclass of prograde incident neutral particles transform upon charging into the toroidal-current/poloidal-field dynamo while a subclass of retrograde neutral particles transform upon charging into the poloidal-current/toroidal-field dynamo that drives a bipolar astrophysical jet. Because θ and α also affect the angle between the velocity vector and the magnetic field at charging, θ and α affect the value of μ and hence the extent to which accreted particles with cyclotron orbits will be mirror trapped to subregions of constant ψ surfaces. For example, if $\alpha = 0$ then variation of the angle of inclination θ for a given $\bar{\rho}_{pericenter}$, and charging radius \bar{R}_* will determine whether the charged particles created upon disintegration of an incoming neutral particle will be normal trapped particles, untrapped particles, drain-hole particles, or Speiser particles.

REFERENCES

- Akers, R. J., Appel, L. C., Carolan, P. G., Conway, N. J., Counsell, G. F., Cox, M., Gee, S. J., Gryaznevich, M. P., Martin, R., Morris, A. W., Nightingale, M. P. S., Sykes, A., Mironov, M., & Walsh, M. J. 2002. Neutral beam heating in the START spherical tokamak. *Nuclear Fusion*, **42**(2), 122–135.
- Bacciotti, F., Ray, T. P., Coffey, D., Eisloffel, J., & Woitas, J. 2004. Testing the models for jet generation with Hubble Space Telescope observations. *Astrophysics and Space Science*, **292**(1-4), 651–658.
- Barnes, C. W., Jarboe, T. R., Marklin, G. J., Knox, S. O., & Henins, I. 1990. The Impedance and Energy Efficiency of a Coaxial Magnetized Plasma Source Used for Spheromak Formation and Sustainment. *Physics of Fluids B-Plasma Physics*, **2**(8), 1871–1888.
- Bellan, P. M. 2000. *Spheromaks: a practical application of magnetohydrodynamic dynamos and plasma self-organization*. London: Imperial College Press.
- Bellan, P. M. 2006. *Fundamentals of Plasma Physics*. Cambridge, UK: Cambridge University Press.
- Bellan, P. M. 2007. Consideration of the relationship between Kepler and cyclotron dynamics leading to prediction of a nonmagnetohydrodynamic gravity-driven Hamiltonian dynamo. *Physics of Plasmas*, **14**. Art. No. 122901.
- Bellan, P. M. 2008. Enrichment of the Dust-to-Gas Mass Ratio in Bondi/J Jeans Accretion/Cloud Systems due to Unequal Changes in Dust and Gas Incoming Velocities. *Astrophysical Journal*, **678**, 1099.
- Bellan, P. M., You, S., & Hsu, S. C. 2005. Simulating astrophysical jets in laboratory experiments. *Astrophysics and Space Science*, **298**(1-2), 203–209.
- Blackman, E. G. 2007. Distinguishing propagation vs. launch physics of astrophysical jets and the role of experiments. *Astrophysics and Space Science*, **307**(1-3), 7–10.
- Chen, F. F. 1984. *Introduction to Plasma Physics and Controlled Fusion, 2nd edition*. New York: Plenum Press. Chapter 2.
- Chrysostomou, A., Hough, J. H., Burton, M. G., & Tamura, M. 1994. Twisting Magnetic Fields in the Core Region of OMC-1. *Monthly Notices of the Royal Astronomical Society*, **268**(2), 325–334.

- Cowling, T. G. 1934. The magnetic field of sunspots. *Monthly Notices of the Royal Astronomical Society*, **94**, 39.
- D'Alessio, P., Calvet, N., & Hartmann, L. 2001. Accretion disks around young objects. III. Grain growth. *Astrophysical Journal*, **553**(1), 321–334. Part 1.
- Dullemond, C. P., & Dominik, C. 2005. Dust coagulation in protoplanetary disks: A rapid depletion of small grains. *Astronomy and Astrophysics*, **434**(3), 971–986.
- Dullin, H. R., Horanyi, M., & Howard, J. E. 2002. Generalizations of the Störmer problem for dust grain orbits. *Physica D-Nonlinear Phenomena*, **171**(3), 178–195.
- Ellison, D. C., Drury, L. O., & Meyer, J. P. 1998. Cosmic rays from supernova remnants: A brief description of the shock acceleration of gas and dust. *Space Science Reviews*, **86**(1-4), 203–224.
- Ferreira, J., & Casse, F. 2004. Stationary accretion disks launching super-fast-magnetosonic magnetohydrodynamic jets. *Astrophysical Journal*, **601**(2), L139–L142. Part 2.
- Ferreira, J., & Pelletier, G. 1995. Magnetized accretion-ejection structures III. Stellar and extragalactic jets as weakly dissipative disk outflows. *Astron. Astrophys.*, **295**, 807–832.
- Geddes, C. G. R., Kornack, T. W., & Brown, M. R. 1998. Scaling studies of spheromak formation and equilibrium. *Physics of Plasmas*, **5**(4), 1027–1034.
- Gloeckler, G., & Geiss, J. 2001. Heliospheric and interstellar phenomena deduced from pickup ion observations. *Space Science Reviews*, **97**(1-4), 169–181.
- Goldstein, H. 1950. *Classical Mechanics*. Reading: Addison Wesley. p. 77.
- Goldston, R. J., & Rutherford, P. H. 1995. *Introduction to Plasma Physics*. Bristol: Institute of Physics Publishing.
- Hartle, R. E., & Killen, R. 2006. Measuring pickup ions to characterize the surfaces and exospheres of planetary bodies: Applications to the Moon. *Geophysical Research Letters*, **33**(5). L05201.
- Hsu, S. C., & Bellan, P. M. 2002. A laboratory plasma experiment for studying magnetic dynamics of accretion discs and jets. *Monthly Notices of the Royal Astronomical Society*, **334**(2), 257–261.

- Hsu, S. C., & Bellan, P. M. 2005. On the jets, kinks, and spheromaks formed by a planar magnetized coaxial gun. *Physics of Plasmas*, **12**(3). 032103.
- Itoh, Y., Chrysostomou, A., Burton, M., Hough, J. H., & Tamura, M. 1999. The magnetic field structure of the DR21 region. *Monthly Notices of the Royal Astronomical Society*, **304**(2), 406–414.
- Jackson, J. D. 1999. *Classical Electrodynamics*. New York: Wiley. 3rd Edition.
- Jarboe, T. R. 1994. Review of Spheromak Research. *Plasma Physics and Controlled Fusion*, **36**(6), 945–990.
- Jura, M. 1980. Origin of Large Inter-Stellar Grains toward Rho-Ophiuchi. *Astrophysical Journal*, **235**(1), 63–65.
- Lamers, H. J. G. L. M., & Cassinelli, J. P. 1999. *Introduction to Stellar Winds*. Cambridge: Cambridge University Press. p.166.
- Lebedev, S. V., Ciardi, A., Ampleford, D. J., Bland, S. N., Bott, S. C., Chittenden, J. P., Hall, G. N., Rapley, J., Jennings, C. A., Frank, A., Blackman, E. G., & Lery, T. 2005. Magnetic tower outflows from a radial wire array Z-pinch. *Monthly Notices of the Royal Astronomical Society*, **361**(1), 97–108.
- Lee, P. 1996. Dust levitation on asteroids. *Icarus*, **124**(1), 181–194.
- Lemaire, J. F. 2003. The effect of a southward interplanetary magnetic field on Störmer’s allowed regions. *Pages 1131–1153 of: Plasma Processes in the near-Earth Space: Interball and Beyond*. Advances in Space Research, vol. 31.
- Lewis, H. R., & Bellan, P. M. 1990. Physical Constraints on the Coefficients of Fourier Expansions in Cylindrical Coordinates. *Journal of Mathematical Physics*, **31**(11), 2592–2596.
- Li, H., Lovelace, R. V. E., Finn, J. M., & Colgate, S. A. 2001. Magnetic helix formation driven by Keplerian disk rotation in an external plasma pressure: The initial expansion stage. *Astrophysical Journal*, **561**(2), 915–923. Part 1.
- Livio, M. 2002. The jet set. *Nature*, **417**(6885), 125–125.
- Longmire, C. L. 1967. *Elementary Plasma Physics*. New York: Interscience. Chapter 3.
- Lovelace, R. V. E. 1976. Dynamo Model of Double Radio-Sources. *Nature*, **262**(5570), 649–652.

- Lovelace, R. V. E., Li, H., Koldoba, A. V., Ustyugova, G. V., & Romanova, M. M. 2002. Poynting jets from accretion disks. *Astrophysical Journal*, **572**(1), 445–455. Part 1.
- Lynden-Bell, D. 2003. On why discs generate magnetic towers and collimate jets. *Monthly Notices of the Royal Astronomical Society*, **341**(4), 1360–1372.
- Lynden-Bell, D., & Pringle, J. E. 1974. Evolution of Viscous Disks and Origin of Nebular Variables. *Monthly Notices of the Royal Astronomical Society*, **168**(3), 603–637.
- Mitchell, C. J., Horanyi, M., & Howard, J. E. 2003. Accuracy of epicyclic description of dust grain orbits about Saturn. *Journal of Geophysical Research-Space Physics*, **108**(A5). 1179.
- Miyake, K., & Nakagawa, Y. 1993. Effects of Particle-Size Distribution on Opacity Curves of Protoplanetary Disks around T-Tauri Stars. *Icarus*, **106**(1), 20–41.
- Pollack, J. B., Hollenbach, D., Beckwith, S., Simonelli, D. P., Roush, T., & Fong, W. 1994. Composition and Radiative Properties of Grains in Molecular Clouds and Accretion Disks. *Astrophysical Journal*, **421**(2), 615–639. Part 1.
- Pringle, J. E. 1981. Accretion Disks in Astrophysics. *Annual Review of Astronomy and Astrophysics*, **19**, 137–162.
- Przygodda, F., van Boekel, R., Abraham, P., Melnikov, S. Y., Waters, L. B. F. M., & Leinert, C. 2003. Evidence for grain growth in T Tauri disks. *Astronomy and Astrophysics*, **412**(2), L43–L46.
- Roberts, D. A., Dickel, H. R., & Goss, W. M. 1997. High-resolution observations of H I Zeeman absorption toward DR 21. *Astrophysical Journal*, **476**(1), 209–220. Part 1.
- Rome, J. A., & Peng, Y. K. M. 1979. Topology of Tokamak Orbits. *Nuclear Fusion*, **19**(9), 1193–1205.
- Schmidt, G. 1979. *Physics of High Temperature Plasmas*. New York: Academic Press.
- Shakura, N. I., & Sunyaev, R. A. 1976. Theory of Instability of Disk Accretion on to Black-Holes and Variability of Binary X-Ray Sources, Galactic Nuclei and Quasars. *Monthly Notices of the Royal Astronomical Society*, **175**(3), 613–632.
- Shebalin, J. V. 2004. Störmer regions for axisymmetric magnetic multipole fields. *Physics of Plasmas*, **11**(7), 3472–3482.

- Shukla, P. K., & Mamun, A. A. 2002. *Introduction to Dusty Plasma Physics*. Bristol: Institute of Physics Publishing.
- Sickafoose, A. A., Colwell, J. E., Horanyi, M., & Robertson, S. 2000. Photoelectric charging of dust particles in vacuum. *Physical Review Letters*, **84**(26), 6034–6037.
- Simonen, T. C., Matsuoka, M., Bhadra, D. K., Burrell, K. H., Callis, R. W., Chance, M. S., Chu, M. S., Greene, J. M., Groebner, R. J., Harvey, R. W., Hill, D. N., Kim, J., Lao, L., Petersen, P. I., Porter, G. D., Stjohn, H., Stallard, B. W., Stambaugh, R. D., Strait, E. J., & Taylor, T. S. 1988. Neutral-Beam Current-Driven High-Poloidal-Beta Operation of the DIII-D Tokamak. *Physical Review Letters*, **61**(15), 1720–1723.
- Speiser, T. W. 1965. Particle Trajectories in Model Current Sheets .I. Analytical Solutions. *Journal of Geophysical Research*, **70**(17), 4219.
- Störmer, C. 1955. *The Polar Aurora*. Oxford: Clarendon Press.
- Tripathi, S. K., Bellan, P. M., & Yun, G. S. 2007. Observation of Kinetic Plasma Jets in a Coronal-Loop Simulation Experiment. *Physical Review Letters*, **98**. Art. No. 135002.
- van Boekel, R., Waters, L. B. F. M., Dominik, C., Bouwman, J., de Koter, A., Dullemond, C. P., & Paresce, F. 2003. Grain growth in the inner regions of Herbig Ae/Be star disks. *Astronomy and Astrophysics*, **400**(3), L21–L24.
- Zelenyi, L. M., Sitnov, M. I., Malova, H. V., & Sharma, A. S. 2000. Thin and superthin ion current sheets. Quasi-adiabatic and nonadiabatic models. *Nonlinear Processes in Geophysics*, **7**(3-4), 127–139.